PHYSIK-DEPARTMENT
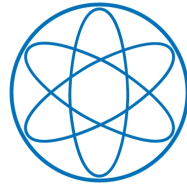
Measurement of
the Charged Pion Polarizability
at COMPASS

Thiemo Nagel

TECHNISCHE UNIVERSITÄT
MÜNCHEN

Measurement of
the Charged Pion Polarizability
at COMPASS

Thiemo Christian Ingo Nagel

Abstract

The reaction $\pi^- + Z \longrightarrow \pi^- + \gamma + Z$ in which a photon is produced by a beam pion scattering off a quasi-real photon of the Coulomb field of the target nucleus is identified experimentally by the tiny magnitude of the momentum transfer to the nucleus. This process gives access to the charged pion polarizabilities α_π and β_π whose experimental determination constitutes an important test of Chiral Perturbation Theory. In this work, the pion polarizability is obtained as $\alpha_\pi = (1.9 \pm 0.7_{\text{stat.}} \pm 0.8_{\text{syst.}}) \times 10^{-4}\,\text{fm}^3$ from data taken with 190 GeV/c hadron beam provided by SPS to the COMPASS experiment at CERN in November 2009 and under the assumption of $\alpha_\pi + \beta_\pi = 0$. The analysis has passed internal peer-review and its outcome has been released as preliminary result by the COMPASS collaboration.

Contents

Chapter 1

Charged pion polarizabilities

1.1 Chiral Perturbation Theory and pion polarizabilities

Quantum Chromodynamics (QCD), the theory of the strong force, holds a fundamental place in our present understanding of particle physics. While it is evaluated at high energies with great success by series expansion in powers of the coupling constant α_s, this approach breaks down at low energies due to the quark confining properties of QCD.

For the treatment of QCD low-energy phenomena such as $\pi\pi$ scattering, an approach using a chiral-invariant effective Lagrangian was proposed in [Wei68], leaning on concepts of current algebra. Since then, the study of the (spontaneously broken) chiral symmetry of QCD with effective field theories has developed into the field of Chiral Perturbation Theory (ChPT) [Leu94] and generally has proven to be successful in the description of light meson masses, interactions and decays. Especially remarkable is the agreement on the level of few percent between calculation and experiment for pion scattering lengths a_0 and a_2 [Gas09].

For the electric and magnetic polarizabilities of the charged pion α_π and β_π which constitute the first non-trivial order in the description of the electromagnetic structure of the charged pions, the situation looks dim in comparison: The evaluation of $SU(2)$ ChPT to $\mathcal{O}(p^6)$ (two loops) first by [Bür96] and since then updated and slightly improved in [GIS06] has lead to the concrete prediction for the difference of the polarizabilities

$$\alpha_\pi - \beta_\pi = (5.7 \pm 1.0) \times 10^{-4}\,\text{fm}^3 \quad [\text{GIS06}], \tag{1.1}$$

but the precision of the experiments in measuring this quantity, the agreement of experimental values among each other and their agreement with theory leave a lot to be desired.

A complete overview of previous polarizability measurements with references to the individual publications is given in Table 1.1 and displayed in Figure 1.1a. Different publications vary between specifying the polarizability α_π and the polarizability difference $\alpha_\pi - \beta_\pi$ in their result description, both of which are considered approximately equivalent and often used interchangeably since the sum $\alpha_\pi + \beta_\pi$ is zero in $\mathcal{O}(p^4)$ ChPT and other theoretical approaches and very small[1] in $\mathcal{O}(p^6)$ ChPT according to [Bür96] and

---

[1][GIS06] report $\alpha_\pi + \beta_\pi = 0.16 \times 10^{-4}\,\text{fm}^3$ which is negligible compared to current experimental and theoretical uncertainties in $\alpha_\pi - \beta_\pi$. An experimental validation is undertaken in [ABB$^+$85], albeit with large statistic and systematic uncertainties.

[GIS06]. In this evaluation, all data are cited in $\alpha_\pi - \beta_\pi$ notation, converted according to $\alpha_\pi - \beta_\pi = 2\alpha_\pi$ where necessary. For comparison of experiments among each other and also with theory, every experiment is assigned a single combined error value by adding quadratically the quoted random and systematic errors (and in one case the model-dependent error). For publications which only quote one error, this error is interpreted as random error and the systematic error is estimated to be of the same size and added quadratically.

In an effort to avoid double-counting (the re-analyses in part are confounded due to shared data sources) and to avoid contested results, only *dedicated* measurements published by experimental groups have been considered for the statistical evaluation. This excludes several re-analyses and combined analyses of $\gamma\gamma \to \pi^+\pi^-$ data which are suffering from fundamental problems according to [Pen95].

The three *dedicated* measurements, most notably by way of $\pi^- Z \to \pi^- \gamma Z$ at Serpukhov (1983) and via $\gamma p \to \gamma \pi^+ n$ measurement at MAMI (2005), are in reasonable agreement (χ^2 CL=67%) with each other as presented in the ideogram in Figure 1.1b, but the combined world average is in serious conflict with the ChPT calculation, differing by 2.6 standard deviations (χ^2 CL=4.4%). To clarify the situation, a new measurement has been called for e.g. by [Ber07].

The work at hand is set to clarify the picture by providing a new and independent experimental data point with an accuracy surpassing that of all previous measurements combined.

	process	$\alpha_\pi - \beta_\pi$
experimental analyses		
Sigma (Serpukhov) [ABB+83]	$\pi^- Z \to \pi^- \gamma Z$	$13.6 \pm 2.8 \pm 2.4$
PACHRA/Lebedev Inst. [ABB+86]	$\gamma p \to \gamma \pi^+ n$	$40 \quad \pm 24$
A2 (MAMI/JGU) [AAA+05]	$\gamma p \to \gamma \pi^+ n$	$11.6 \pm 1.5 \pm 3.0 \pm 0.5$
re-analysis D. Babusci *et al.* [BBG+92]		
PLUTO (PETRA/DESY) [B+84]	$\gamma\gamma \to \pi^+\pi^-$	$38.2 \pm 9.6 \pm 11.4$
DM1 (DCI/Orsay) [MP87]	$\gamma\gamma \to \pi^+\pi^-$	34.4 ± 9.2
DM2 (DCI/Orsay) [MP87]	$\gamma\gamma \to \pi^+\pi^-$	52.6 ± 14.8
Mark II (PEP/SLAC) [BBG+90]	$\gamma\gamma \to \pi^+\pi^-$	4.4 ± 3.2
re-analysis Donoghue and Holstein [DH93]		
Mark II	$\gamma\gamma \to \pi^+\pi^-$	5.3 ± 3.5^2
combined analysis Kaloshin *et al.* [KS94]		
Mark II, Crystal Ball (DESY) [MAB+90]	$\gamma\gamma \to \pi^+\pi^-$	5.3 ± 1.0^3
combined analysis Fil'kov *et al.* [FK06]		
Mark II, TPC/2γ [A+86], CELLO [B+92], VENUS [Y+95], ALEPH [H+03], BELLE [N+05]	$\gamma\gamma \to \pi^+\pi^-$	$13.0^{+2.6}_{-1.9}$

Table 1.1: previous measurements of the charged pion polarizabilities (α_π converted to $\alpha_\pi - \beta_\pi$ where necessary)
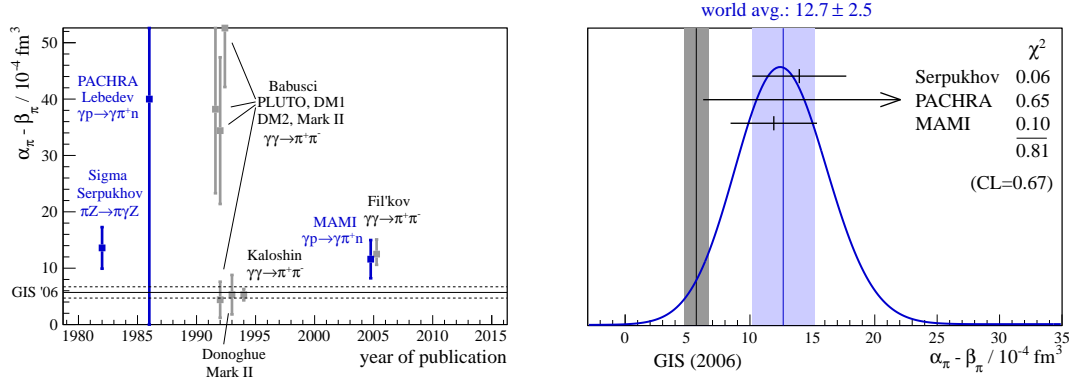
(a) Overview of previous polarizability measurements: Dedicated experimental measurements are shown in blue whereas re-analyses and combined analyses are indicated in grey.

(b) Ideogram of the dedicated experimental measurements in they style used by the Particle Data Group. The quoted confidence level refers to the agreement of the experiments with each other. (A conceptual description is given in [N+10] Chapter 5.2.2.)

Figure 1.1: Previous measurements of $\alpha_\pi - \beta_\pi$: The ChPT prediction by [GIS06] and its error margins are indicated by the solid/dashed lines and the grey band respectively.

1.2 Pion polarizabilities at COMPASS

For the lack of pion targets, it is the process of a beam pion scattering off a quasi-real photon from the Coulomb field of the nucleus (cf. Figure 1.2)

$$\pi + \gamma^* \rightarrow \pi + \gamma \tag{1.2}$$

that allows the measurement of the charged pion polarizabilities with the least dependence on theoretical models [Pen95]. Belonging to the class of hadron-γ^* interactions commonly referred to as Primakoff processes with regard to [Pri51], this reaction often is described as Primakoff-Compton scattering. The realization of the factorizability of these processes into the cross section of their real-photon counterpart and the density of virtual photons however goes back to [vW34, Wil34]. An exhaustive treatment of the kinematics of the Primakoff-Compton process is presented in [Fri12b].

In this work as in general practice, the virtual photon is formally treated as an incom-

---

[2]Donoghue and Holstein in [DH93] present a theoretical calculation of α_π and β_π and compare their result with the Mark II measurement in [MP87], concluding that both are in agreement. Following [GIS06], this is interpreted as extraction of α_π from Mark II data. No confidence level is quoted, but the authors mention that the Mark II measurement could not distinguish between polarizability values 50 % smaller or larger than what they have obtained and note that their evaluation of Mark II would yield somewhat larger errors than the evaluation in [BBG+92]. In accordance with these statements, an error of 3.5×10^{-3} fm has been assigned.

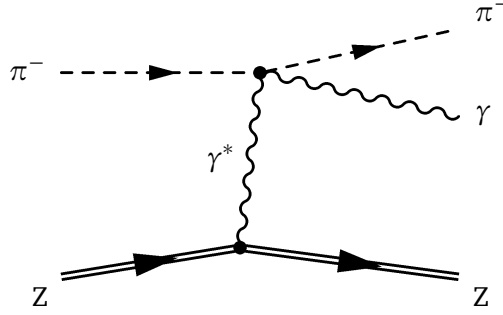[3]This result is heavily criticised in [Pen95].

Figure 1.2: Primakoff-Compton scattering

ing particle so that energy and momentum conservation is written as:

$$\begin{pmatrix} E_{\text{beam}} \\ \vec{p}_{\text{beam}} \end{pmatrix} + \begin{pmatrix} E_{\text{q}} \\ \vec{q} \end{pmatrix} = \begin{pmatrix} E_{\pi} \\ \vec{p}_{\pi} \end{pmatrix} + \begin{pmatrix} E_{\gamma} \\ \vec{p}_{\gamma} \end{pmatrix} \tag{1.3}$$

Explicitly measured quantities are the direction of the incoming beam (although an indirect measurement of its energy is discussed in Section 3.5) and 4-vectors of the scattered pion and the emitted photon (which is assumed to originate from the primary vertex).[4] For the occurring momenta of the virtual photon of up to $|\vec{q}| \approx 30\,\text{MeV}$, the measurement of the recoiling nucleus is out of reach of COMPASS instrumentation so that $\vec{q}$ must be inferred from momentum conservation as

$$\vec{q} = \vec{p}_{\pi} + \vec{p}_{\gamma} - \vec{p}_{\text{beam}} \tag{1.4}$$

wherein the beam momentum vector itself is inferred through energy conservation via

$$\vec{p}_{\text{beam}} = \underbrace{\frac{\vec{p}_{\text{beam}}}{|\vec{p}_{\text{beam}}|}}_{\text{measured}} \cdot \sqrt{(E_{\pi} + E_{\gamma})^2 - m_{\pi}^2 c^4} \tag{1.5}$$

exploiting the fact that the corresponding recoil energies of the heavy nickel nucleus reach only up to $\sim 8\,\text{keV}$ and thus lie many orders of magnitude below the experimental resolution and may safely be disregarded.

With momentum and energy conservation laws applied in the calculation of the set of kinematic variables, the kinematics obtained are self-consistent. The achieved resolution in q is sufficient to disentangle electromagnetic and strong interactions to a large extent.

The measurement of the charged pion polarizability by this method was featured among the physics goals already at the inception of the COMPASS experiment in [B+96]. In [Ku01] the simulation of the process has been pursued to prepare the measurement which however started with muon beam in 2002. At the end of the 2004 beam time, a short hadron pilot run with an effective recording time of few days supplied Compton-Primakoff events in quantities that already would have been sufficient to exceed the accuracy of the Serpukhov measurement. Yet, the data quality turned out to be inadequate

---

[4]In contrast to hadron beam data, the events recorded with muon beam include a measurement of the momentum of the incoming muon by the Beam Momentum Station (BMS, cf. Section 2.2) which has proven useful in the calibration of the second electromagnetic calorimeter as treated in Section 3.2. The BMS is removed from the beam during hadron beam to reduce the amount of material in the beam.

for the publication of a result, as the analyses of [Gus10] and [Din10] have shown, while at the same time laying the groundwork for many improvements that have been realized in the Primakoff part of the 2009 beam time. While the present analysis is focused on the data sample obtained in 2009, in effect comprising about two weeks of measurements, an extended Primakoff campaign was proposed in [G⁺10] to expand the precision and the reach of the measurements. The aims of the 2012 Primakoff beam time, that at the time of writing just has finished, include separate determination of α_π and β_π without the constraint of $\alpha_\pi + \beta_\pi = 0$ and the measurement of quadrupole polarizability terms, polarizability s-dependence and also kaon polarizability.

1.3   Conventions and nomenclature

In all contexts in this work, α_π and β_π are employed to denote the electric and magnetic polarizabilities of the *charged* pion. q^2 is used as a shortcut for $\vec{q}^2$ and q as a shortcut for $|\vec{q}|$, likewise for p. Physical quantities indexed with π or μ, as in E_π or p_μ pertain to the respective particle after scattering on the target. The index *beam* is used to refer to the incoming particle, eg. as in E_{beam}.

All plots are shown with full polarizability cuts applied, except where specified otherwise, and except for cuts on quantities which are represented on the coordinate axes of the plot. In case of the latter, red dashed lines are used to indicate the cut positions. Unless declared differently, data points are drawn in blue and with error bars and simulated data are drawn as red lines without error bars.

COMPASS is using a right-handed coordinate system whose origin resides (approximately) in the target. The Y-coordinate is pointing upwards and the Z-coordinate is defined as the direction of the beam momentum.

Chapter 2

Experimental setup

COMPASS is a fixed target experiment located at the North Area of CERN where it is supplied with various kinds of secondary and tertiary beams from the SPS by way of the M2 beam line. The spectrometer itself (cf. Figure 2.3 and Figure 2.2) is designed as a succession of two similar spectrometers stages called Large Angle Spectrometer (LAS) and Small Angle Spectrometer (SAS) which are arranged one after another to allow precise measurement of charged and neutral particles of a wide range of momenta. The two stages feature spectrometer magnets of increasing strength and each of the stages is equipped with tracking detectors and electromagnetic and hadronic calorimetry, the calorimeters of the first stage featuring a central hole that matches the acceptance of the second stage.

The first spectrometer stage allows identification of secondary particles by means of a RICH detector and further PID capability is supplied by calorimetry and a dedicated muon system at the

Figure 2.1: overview of CERN accelerators (not to scale), from [CER]

downstream end of the experimental setup. Beam PID with CEDARs is delineated in Section 2.3.

Selected features that are of specific relevance to the work at hand are described in the following sections. A comprehensive account of the COMPASS spectrometer is given in [A⁺07], upgrades to the apparatus for the hadron beam times 2008–2009 are described in [COM12].
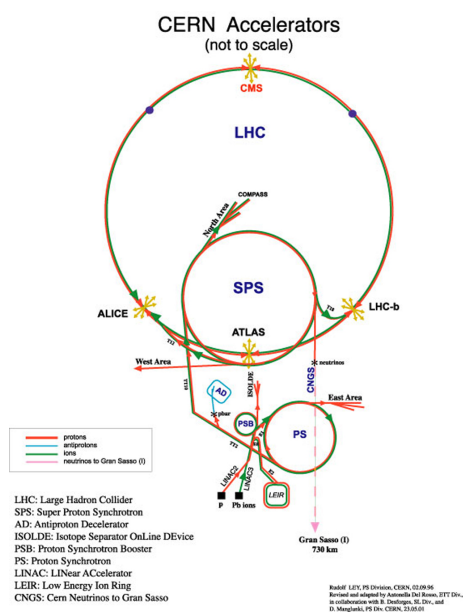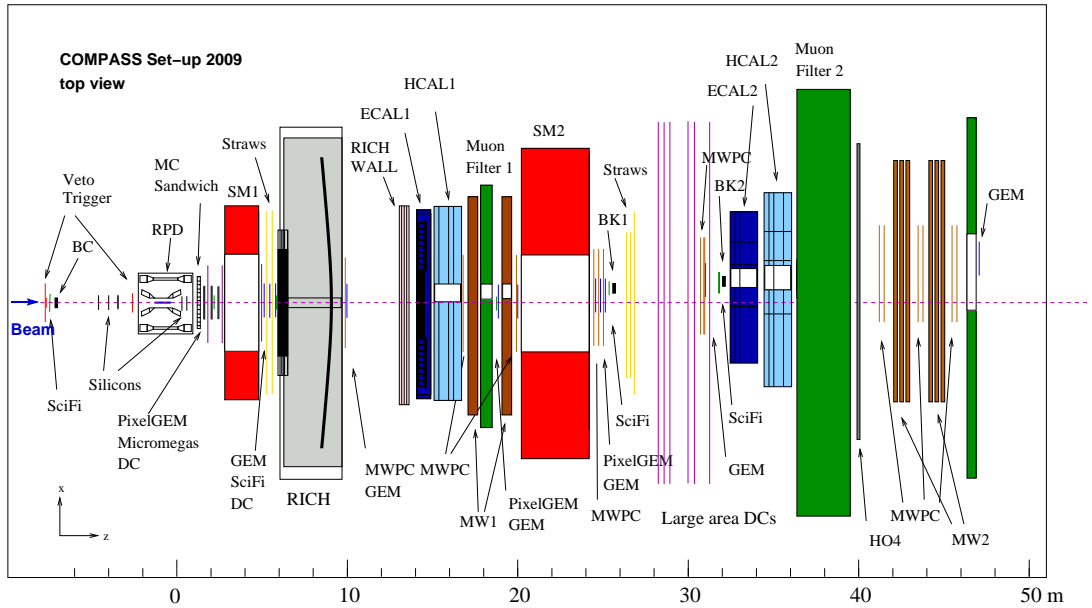
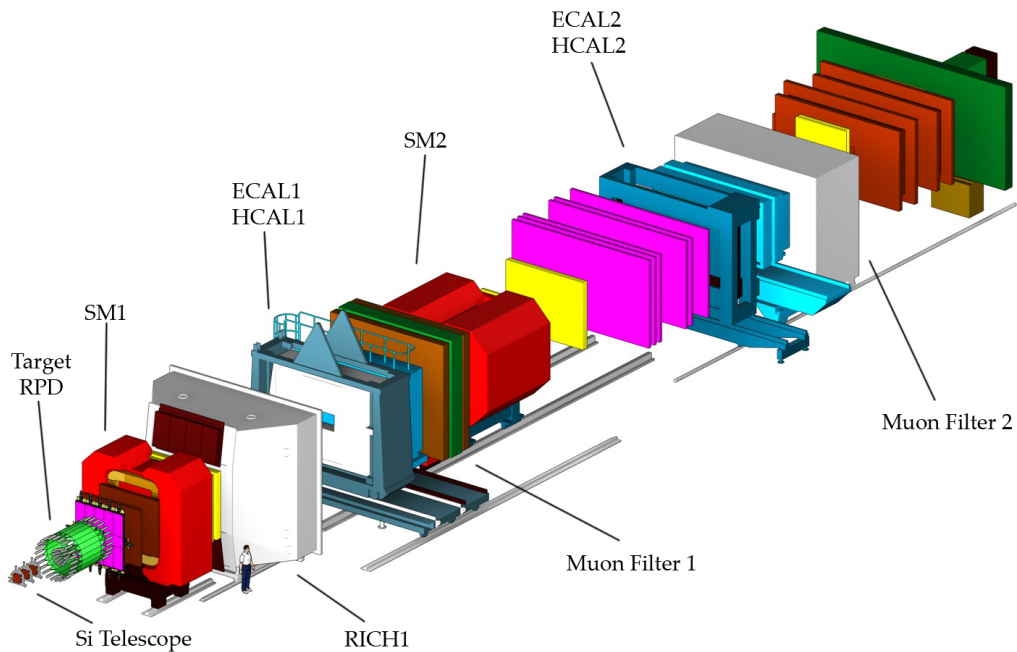Figure 2.2: top view of the COMPASS spectrometer, cut at beam axis, from[COM12]

Figure 2.3: three-dimensional view of the COMPASS spectrometer, from [COM12]

2.1 Beam

In the polarizability analysis, data taken with a negative hadron beam of 190 GeV/c momentum and a tertiary beam of negative muons of the same nominal momentum have been used.

During the 2009 Primakoff period, the SPS was following a complex cycle comprised of several injection-acceleration-extraction sequences supplying different users of the beam. From the point of view of the COMPASS, the cycle length was ∼40 s with an extraction period of ∼10 s, the latter commonly called *spill*, *burst* or *pulse*. Running at 400 GeV/c momentum, SPS was delivering an average of 1.5×10^{13} protons per pulse onto the primary target T6 for which beryllium had been selected[1].

For data recording with hadron beam, the secondary particles generated at T6 are transported to the COMPASS target by the M2 [M2] beam line of which a detailed drawing is presented in Figure 2.5. Negative charge and 190 GeV/c (nominal) beam momentum are selected by appropriate current settings of the bending magnets. The resulting hadron beam consists mostly of π^-, but small contributions of K^-, $\bar{p}$, e^- and μ^- are known to be present. The fraction of K^- among the beam hadrons at the position of the COMPASS target is calculated to be 2.4 % by the author of the present work in [NFP08] using data from [ABD$^+$80] and taking into account decays along the beam line. The contribution of anti-protons is 0.6 %. Exact numbers for the lepton content are not known, but the lepton fraction must be low as they only are produced through weak processes, either in the primary target or in decays of beam hadrons.
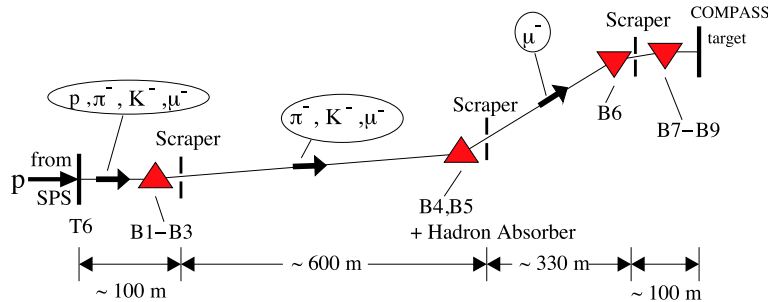
Figure 2.4: M2 beam line schematics in *muon* configuration (adapted from [vH02])

Nevertheless, for the last 2.5 days of data taking, the electron target which is built of 5 mm lead was inserted into the beam line (at ∼670 m) which causes electrons to loose energy via bremsstrahlung so that they are not transported by the beam optics anymore. The suppression factor for electrons effected this way was determined to be 3.5 ± 0.7 by [Gus11]. For the analysis, electron-Compton events are suppressed by the cut on transverse momentum (cf. Section 4.9).

To obtain muon beam, 9.9 m of beryllium are moved into the beam line at B4 after approximately 700 m of decay line (cf. Figure 2.4), effectively removing the hadron part of the beam while the muon part stemming from decays of hadronic beam particles pass through it with moderate energy loss, yielding a tertiary beam whose divergence and momentum spread are considerably larger than that of the hadron beam, though.

---

[1]Other choices are silicon and air.

Figure 2.5: M2 beam line (by [Gat, Bis])

2.2 Beam Momentum Station

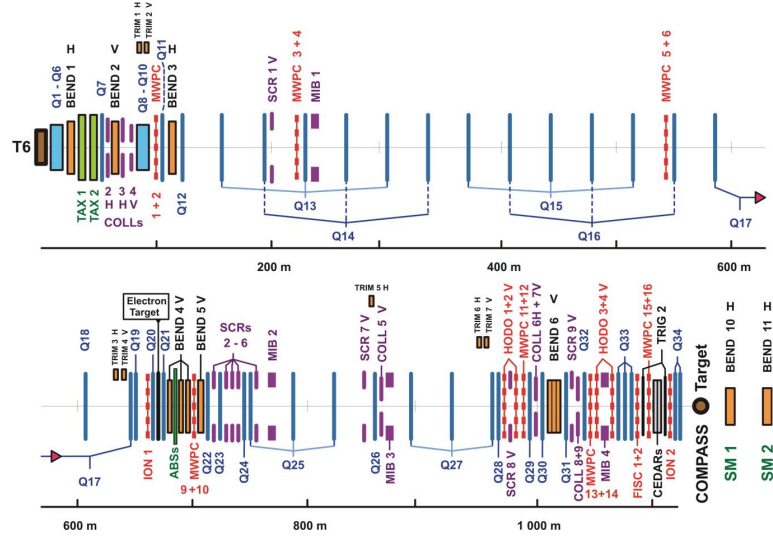During the recording of data with muon beam, the momentum of the beam particles is measured using the Beam Momentum Station (BMS) which consists of 6 planes of scintillating fibers that are placed around the B6 bending magnet of the M2 beam line approximately 100 m upstream of the COMPASS target. However, for data taking with hadron beam, these detectors are removed to minimize the amount of hadronic interactions in the beam line, which until recently has left the experiment without a possibility to determine the momentum of the incoming hadrons safe of assuming the nominal value of the beam momentum. Yet, in Section 3.5 a method for the determination of the energy of the incoming hadrons through beam parameter correlations developed by [Fri12a] and [Krä12] is introduced.

2.3 CEDARs

The composite nature of the beam makes beam PID capabilities highly desirable. To that end, two CEDAR[2] detectors [BMP78, BMP⁺82] have been provided and operated by CERN and read out via the COMPASS DAQ. A CEDAR detector consists of a pressure vessel with helium gas at approx. 10 atmospheres inside which parallely entering beam particles undergo Cherenkov radiation that with a complex arrangement of optical elements is focused on a set of photomultiplier tubes behind a ring diaphragm at the upstream edge of the detector (cf. Figure 2.6). Variation of the gas pressure changes the diameter of the ring of Cherenkov photons that is projected onto the ring diaphragm for a certain type of particle at a certain energy so that in a approximately monoenergetic beam, each detector may be tuned to register a specific particle by selecting a specific pressure.

---

[2]**Ch**Erenkov **D**ifferential counters with **A**chromatic **R**ing focus
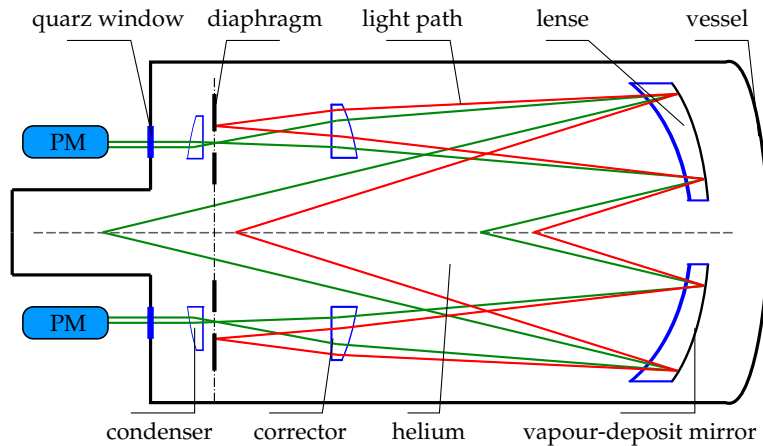
Figure 2.6: CEDAR design schema, from [Jas12]

For the 2009 Primakoff data taking, both CEDARs have been set on kaons to attain the highest possible kaon suppression for the polarizability measurement. Further discussion is held in Sections 4.5 and 6.2.

2.4 Target region

As target for Primakoff-Compton scattering a solid nickel disk of 4.2 mm thickness corresponding to 28.5 % of a radiation length has been used. It is composed of the natural isotope distribution in the earth's crust, dominated by ^{58}Ni (abundance: 68.1 %) and ^{60}Ni (abundance: 26.2 %). Among other considerations, the target material has been selected for its high fraction of spin-0 nuclei of 98.9 % which allows to disregard spin effects in the theoretical treatment of the cross section [NuD12]. Two auxiliary targets made of tungsten with thicknesses of 50 μm and 25 μm (1.4 % X_0 and 0.7 % X_0) were placed 40 cm downstream of the principal target, spaced 5 cm apart. All targets have a diameter of 5 cm to ensure generous overlap with the incoming beam distribution. (For the polarizability analysis, interactions in the auxiliary targets are removed by a cut on the primary vertex position as described in Section 4.6.)

As depicted in Figure 2.7, upstream and downstream of the target a total of 5 stations of cryogenic silicon micro-strip detectors are placed, delivering spatial accuracies of 4–11 μm to provide excellent vertex resolution which is crucial for the precise determination of the momentum transfer to the nucleus. A detailed overview over the COMPASS silicon detectors is given in [Gra12] whereas some individual contributions may be found in [Bic11, Lee11, Zim11].

The COMPASS Recoil Proton Detector (RPD, labelled as TOF scintillators in Figure 2.7) consists of two cylindrical formations of plastic scintillators arranged concentrically around the beam axis at the target position and is commonly used to record the recoiling nucleus during measurements with hydrogen target. Since the nuclear recoil momenta in Primakoff-Compton scattering are much below the sensitivity threshold of the RPD, it is used as a veto in the polarizability analysis to suppress a part of the strong
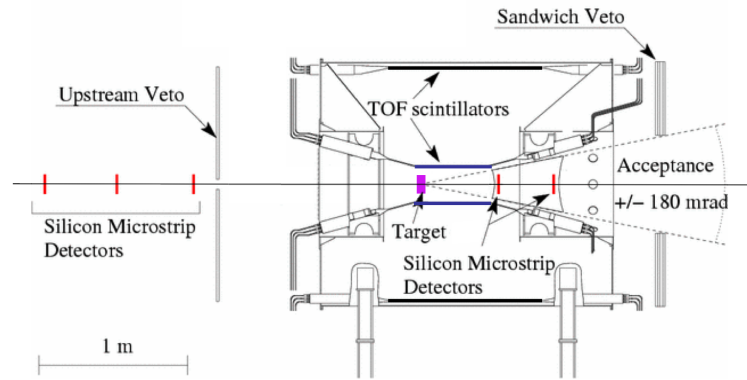
Figure 2.7: drawing of the target region (adapted from [COM12])

interactions.

2.5 Calorimetry

The second electromagnetic calorimeter (ECAL2) is of central importance of the polarizability measurement. It is placed at the end of the Small Angle Spectrometer, approximately 34 m downstream of the target, to allow for sufficient lever arm to determine photon angles to a precision of $\sim$0.2 mrad. With the exception of a small beam hole, the area of 2.5 m × 1.8 m is covered by 64 × 48 calorimeter cells (cf. Figure 2.8) made of different types and materials (shown in Figure 2.9) following the different demands of radiation hardness at different positions.

Figure 2.8: layout of ECAL2, from [COM12]

Figure 2.9: different types of calorimeter blocks [Pol]: lead glass, shashlik, radiation-hard lead glass (from top to bottom)

2.6 Trigger

Two dedicated "Primakoff" triggers have been used to perform the broadest-possible selection of potentially interesting interactions while still keeping within the rate capability of COMPASS front-ends and DAQ of ∼30 kHz. The triggers were configured with a minimum-bias component (called LOWT2) in coincidence with the passin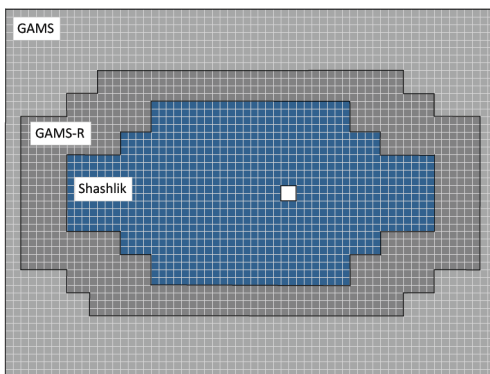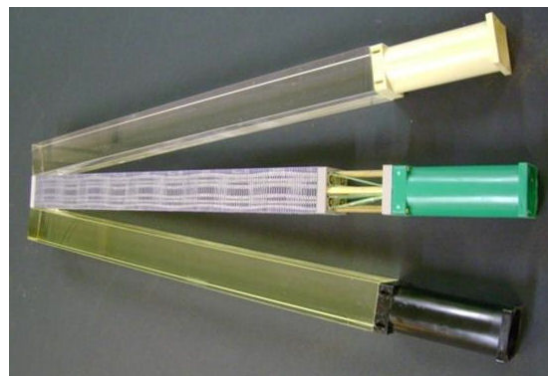g of thresholds for energy deposited in the central part of ECAL2, of which two different have been used for the two Primakoff triggers [B+12b].

The LOWT2 minimum bias part was realized as the alternative Beam Trigger (aBT) in anti-coincidence with a veto system consisting of hodoscope vetoes to suppress beam halo (here denoted as HO), a sandwich (SW) veto and the coincidence of two beam killer scintillators (BK1 and BK2).

The alternative Beam Trigger ensures the presence of a beam track that is pointing very approximately at the target by requiring coincidence of a disc-shaped plastic scintillator of 32 mm diameter called Beam Counter (BC) placed ∼6 m upstream of the target with a signal in FI01X, which is a scintillating fibre detector with an active area of approximately 4 cm × 4 cm placed ∼7 m upstream of the target.

Designed to suppress interactions which (partly) fall outside of COMPASS acceptance, the sandwich veto [SDD+11, S+11] is situated ∼2 m downstream of the target and features a central hole matching the angular acceptance of the spectrometer.

The ECAL2 energy deposition into the 12 × 12 central blocks (with the exception of 8 blocks that are close to the beam hole) is determined by fast digital summation [HFK+11] in the front-end electronics (cf. Figure 2.10) which are also used for the read-out of the calorimeter. Independent trigger signals are generated when the nominal energy thresholds of 40 GeV and 60 GeV respectively are exceeded. The effective value of the threshold corresponding to the 60 GeV nominal setting has been determined as $E_0 = 65$ GeV together with the resolution $\Delta E = 2$ GeV in [HFK+11] by fit of a Fermi function

$$f(E) = \frac{2\,\epsilon}{1 + \exp(\frac{E_0 - E}{\Delta E})} \tag{2.1}$$

to the fraction of events triggered with 60 GeV nominal setting over those with 40 GeV nominal setting depending on the total energy deposit as shown in Figure 2.11.

Summarizing the previous paragraphs, the Primakoff triggers may be described by the following shorthand notation in which the ∧ operator is used to denote coincidence and in combination with ¬ anti-coincidence:

Prim1: (ECAL2 > 40 GeV) ∧ FI01X ∧ BC ∧ ¬HO ∧ ¬SW ∧ ¬(BK1 ∧ BK2)

Prim2: (ECAL2 > 60 GeV) ∧ FI01X ∧ BC ∧ ¬HO ∧ ¬SW ∧ ¬(BK1 ∧ BK2)

During the recording of physics data, both triggers were used, Prim1 being pre-scaled by a factor of two to limit the data rate.

2.7 Data recording, processing and analysis

The present analysis is based on data taken in November 2009 (period W45). After commissioning of the ECAL2 trigger had been completed, hadron and muon beam running
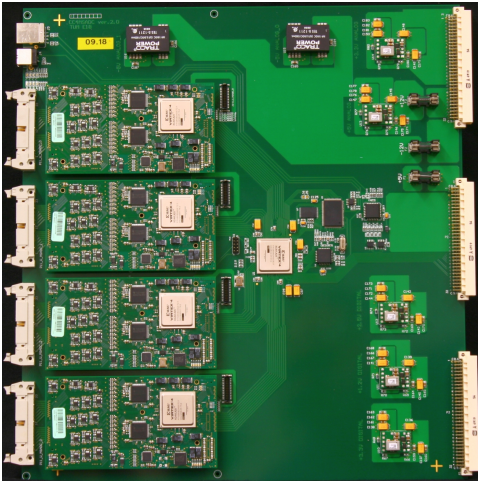
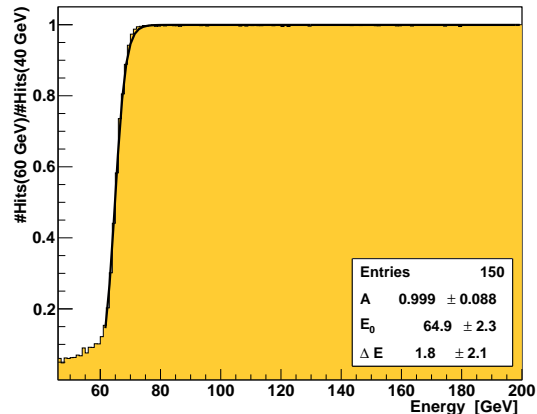Figure 2.10: MSADC read-out carrier card on which 4 mezzanine cards have been mounted (from [HFK$^+$11])

Figure 2.11: fraction of events triggered with 60 GeV nominal setting over those with 40 GeV nominal setting depending on the total energy deposit (from [HFK$^+$11])

have been interleaved for a total of approximately two weeks of physics data taking: one week of hadron beam was followed by two days of muon beam and another four days of hadron beam.

For practical reasons, data recording at COMPASS is organized in *runs* comprised of up to 200 *spills* (cf. Section 2.1) and lasting up to ∼2 hours which are taken in identical conditions, assigned consecutive numbers and documented in an electronic logbook. For the present analysis, 99 runs with hadron beam and 22 runs with muon beam have been selected out of the range 81883–82154 according to their quality as documented in the logbook for processing with the CORAL[3] reconstruction software, which in COMPASS parlance is called "mDST[4] production". After having gone through a rapid succession of several cycles of test productions, the *hadron2009t68* (muon) and *hadron2009t70* (hadron) productions from August–September 2011 have been considered adequate for physics analysis, the result of which is presented in this work. Further details of the data productions may be found in the COMPASS wiki [NBG12].

As a part of this analysis, pre-selection of events was performed with PHAST[5] [PHA] on the E18 computing cluster [E18]. The subsequent interactive analysis was carried out with the ROOT parallel processing facility PROOF [ROO] on individual multi-core machines at E18. The C++ source codes created for the analysis at hand are available from the author upon request.

---

[3]The **CO**MPASS **R**econstruction and **A**nalysis **L**ibrary [COR] performs most event reconstruction tasks including decoding, clustering, tracking, vertexing, calorimeter cluster fit and to some extent particle ID, storing its results in compressed data files called mDSTs.

[4]**m**ini **D**igital **S**ummary **T**ape

[5]**PH**ysics **A**nalysis **S**oftware **T**ools

Chapter 3

Calibrations

Due to the high demands on accuracy of the polarizability which at COMPASS are un-precedented, a large amount of calibrations in the widest sense have proven necessary, many of which have been developed specifically for the purpose of the polarizability measurement but certainly are for the benefit of future measurements as well.

3.1   ECAL2 pre-production calibrations

The second electromagnetic calorimeter ECAL2 is an intricate device and the joint efforts of a calorimeter working group inside COMPASS, stacking calibration upon calibration over the course of many months, have been necessary to reach a level of accuracy that is satisfactory for the polarizability measurement.

At the begin of the Primakoff beam time, basic per-cell energy calibration coefficients have been obtained from calibration with electron beam. The drift over time of the ampli-fications of the individual cells was monitored by LED pulses injected into the cells during the *off-spill* period, i.e. in the time between two successive *spills* (cf. Section 2.1) and a derived correction factor subsequently applied to the electron beam calibrations *distinct for every spill*.
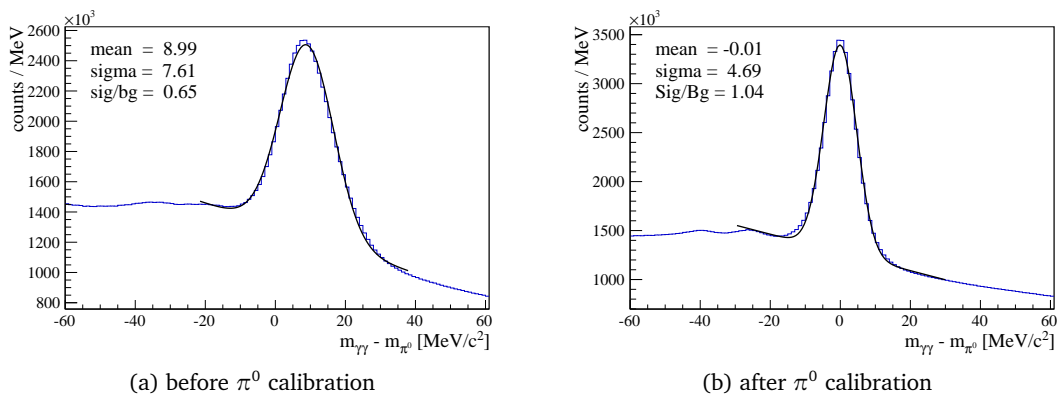

(a) before π^0 calibration   (b) after π^0 calibration

Figure 3.1: π^0 mass aggregated over all calorimeter blocks, by [Ger12]

The π^0 mass provides a useful gauge for further refinement of the calibrations and in an iterative approach two sets of non-linear corrections have been produced on a per-cell level by [Ger12]. The first set of corrections addresses the non-linearity in the energy response whereas the second set compensates variations depending on the event time *relative to the beginning of the spill* which are believed to stem from heating up of the electronics. The benefit of the π^0 calibration is summarized in Figures 3.1 and 3.2.

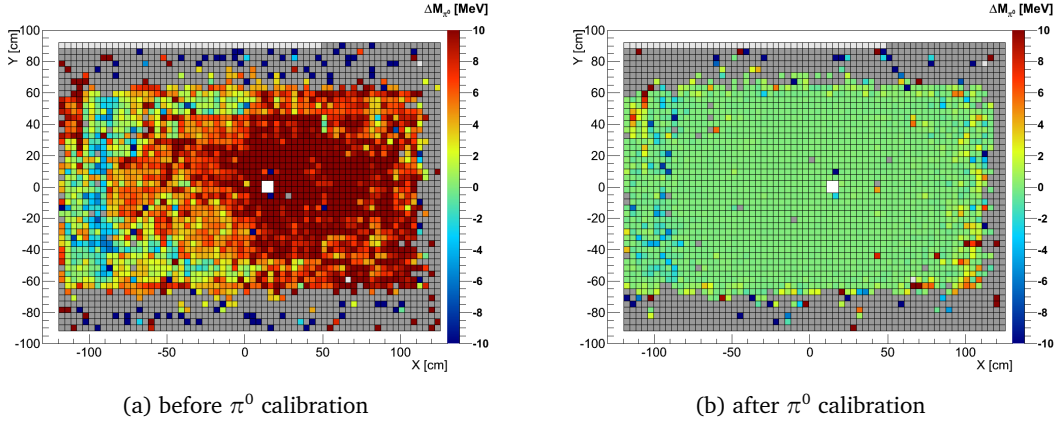(a) before π^0 calibration   (b) after π^0 calibration

Figure 3.2: π^0 mass depending on calorimeter block, by [Ger12]

As the last step of processing inside the reconstruction software CORAL, after all of the aforementioned calibrations have been applied, showers are fitted to the calorimeter clusters in an implementation by [Uhl] which also includes specific post-corrections of the shower position depending on the position of the shower centre relative to the cell boundaries.

3.2 ECAL2 post-production calibrations

During the course of the Primakoff analysis it was realized that while the π^0 calibrations certainly are successful for low photon energies, they afford limited reach towards the high energies that are most important for the measurement of the pion polarizability. Also a relevant dependency of the reconstructed energy on the photon position relative to the cell boundaries has been observed.

The data recorded with muon beam has proven especial useful to generate ECAL2 post-production calibrations (generated and applied from within the analysis code) because the measurement of the momentum of the incoming muon in the Beam Momentum Stations together with the track momentum of the scattered particle measured in the spectrometer allows indirect access to the energy of the shower in ECAL2 in the Primakoff-Compton scattering $\mu^- \gamma^* \to \mu^- \gamma$ through energy conservation.

Figure 3.3a shows the relation between energy balance and the inferred energy of the photon in which remaining non-linearity is visible as a falling slope and the position-dependence of the energy measurement is expressing itself as a vertical broadening of the line, especially visible at high photon energies.
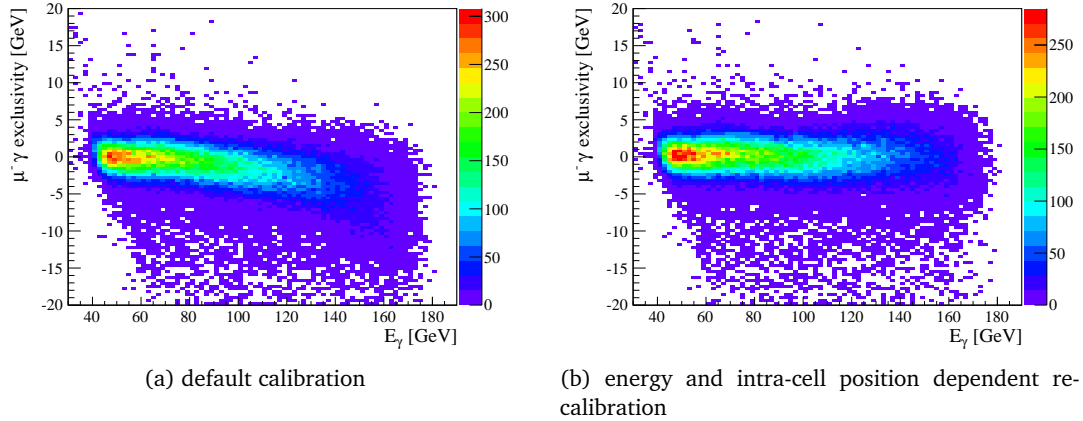
(a) default calibration

(b) energy and intra-cell position dependent re-calibration

Figure 3.3: t68 real data: $\mu^-\gamma$ exclusivity versus inferred photon energy.

Even when manually re-calibrating the energy dependence by adding a 1st order polynomial in photon energy, the position dependence of the reconstructed photon energy prevents a narrow exclusivity cut. Depending on shower position, reconstructed energies vary approximately between -13 GeV and +8 GeV relative to the expected value, as illustrated in Figure 3.4a.

Therefore, to improve energy resolution, a more sophisticated three-dimensional correction which depends on shower energy and intra-cell shower (X, Y) position was derived from muon data. The spatial part of the correction consists of a broad component which slowly varies across the cell and a sharply localized component describing the decrease of visible energy at the steel rods that tie together the shashlik stack at $(X, Y) = (9.5\,\text{mm}, 9.5\,\text{mm})$, as displayed exemplary in Figure 3.5 in good agreement with the technical drawing in Figure 3.6. It is necessary to treat X and Y dimensions separately to achieve the greatest spatial homogeneity in the re-calibrated data, an effect that might be attributed to gravity pressing together the calorimeter blocks in the vertical direction.

Figure 3.7 shows the correction E_{corr} plotted against the uncorrected shower energy. The effect of the re-calibration on the exclusivity peak is exhibited in Figure 3.8a: The width as obtained from fit with a Gaussian is decreased from $\sigma = 2.7\,\text{GeV}$ to $2.4\,\text{GeV}$, but much more importantly, the re-calibration is quite efficient at correcting the non-Gaussian tail to lower energies which features prominently in the uncorrected data. As a consequence, a much tighter exclusivity cut may be used in the extraction of the polarizability, which is useful to suppress non-exclusive background.

The re-calibrated shower energy is given by $E'_\gamma = E_\gamma + E_{\text{corr}}$ in units of GeV whereas

$$E_{\text{corr}} = p_0 + p_1 x^2 + p_2 y^2 + p_4 \exp\left(-\frac{(x - p_6)^2 + (y - p_7)^2}{2p_5^2}\right) \tag{3.1}$$

with variables x and y denoting the shower position in cm with respect to the center of the cell. The energy-dependence of the parameters p_0 ... p_7 is expressed through the

(a) linear energy re-calibration

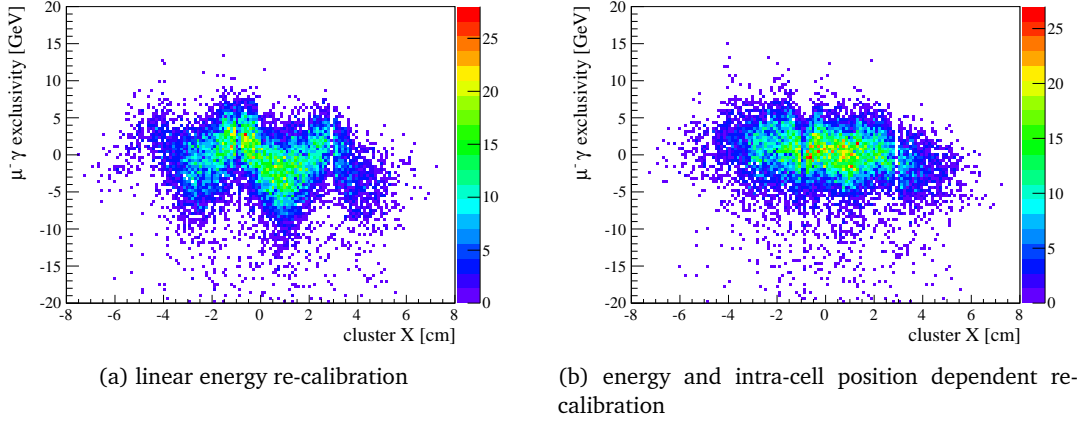(b) energy and intra-cell position dependent re-calibration

Figure 3.4: $\mu^-\gamma$ exclusivity plotted against X-position of ECAL2 shower for photons within the range $133\,\text{GeV} < E_\gamma < 152\,\text{GeV}$.

normalized shower energy $x_{190} = \frac{E_\gamma}{190\,\text{GeV}}$. The values of the individual parameters are:

$$p_0 = 9.57965 \quad + 6.42201 \quad \arctan(7.38429\,(x_{190} - 0.749578)) - 0.74$$
$$p_1 = -1.89692 - 1.2888 \quad \arctan(8.79757\,(x_{190} - 0.738527))$$
$$p_2 = -1.61223 - 1.13902 \quad \arctan(9.43193\,(x_{190} - 0.759991))$$
$$p_4 = -2.57235 + 15.9715 \quad x_{190}$$
$$p_5 = 0.214072 \quad - 0.202193\,x_{190}$$
$$p_6 = 1.00$$
$$p_7 = 0.97$$

The systematics of ECAL2 are somewhat different for muon and hadron beam data due to what is believed a heating-up effect observed for hadron data. But since this effect is corrected by application of time-in-spill dependent calibrations at the time of event reconstruction as described in Section 3.1, it is plausible to assume that the re-calibration obtained from muon data may be applied to hadron data identically. This notion is supported by experimental evidence: Upon re-calibration, the width of the $\pi^-\gamma$ exclusivity peak as obtained from fit of a Gaussian decreases from $\sigma = 2.8\,\text{GeV}$ to $2.6\,\text{GeV}$ and again the tail to lower energies — which for pion data sits atop an otherwise flat background distribution — is substantially reduced, as shown in Figure 3.8b.
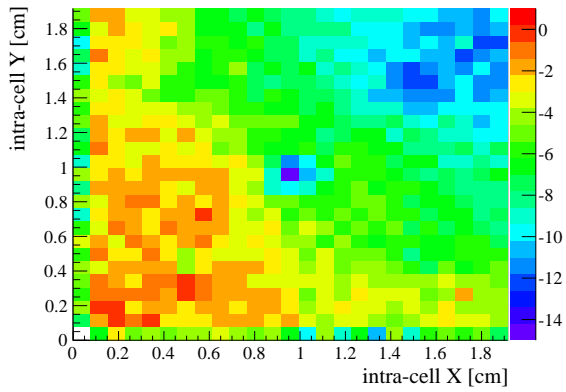
Figure 3.5: Profile of energy deviations shown for 1/4 of a shashlik block and for muon data photons within the range $133\,\text{GeV} < E_\gamma < 152\,\text{GeV}$.
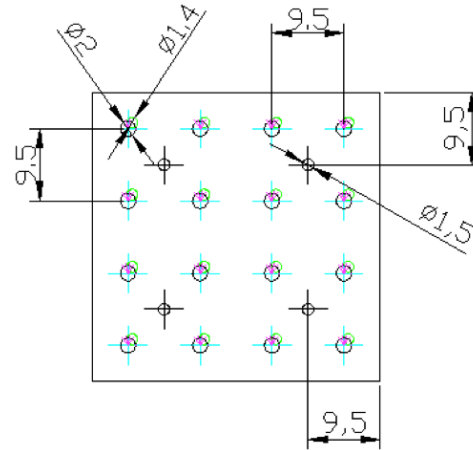
Figure 3.6: Technical drawing of a full shashlik cell to be compared with the figure to the left.
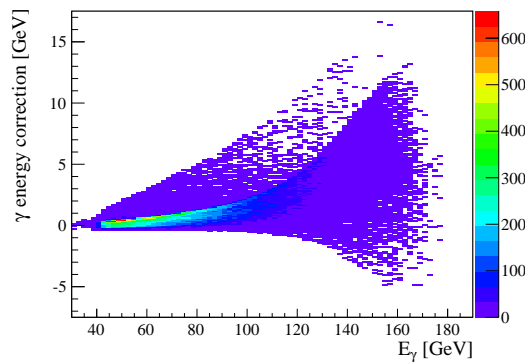
Figure 3.7: Energy correction versus uncorrected shower energy.

(a) $\mu^-\gamma$ (b) $\pi^-\gamma$
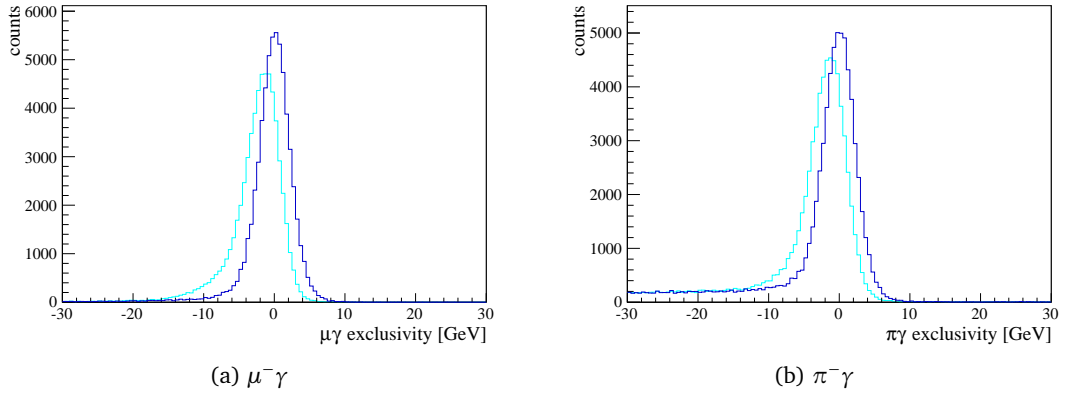
Figure 3.8: energy balance with standard ECAL2 calibration (cyan) and after energy and intra-cell position dependent re-calibration (blue)

(a) ECAL2 "production" calibrations   (b) energy and intra-cell position dependent re-calibration of ECAL2
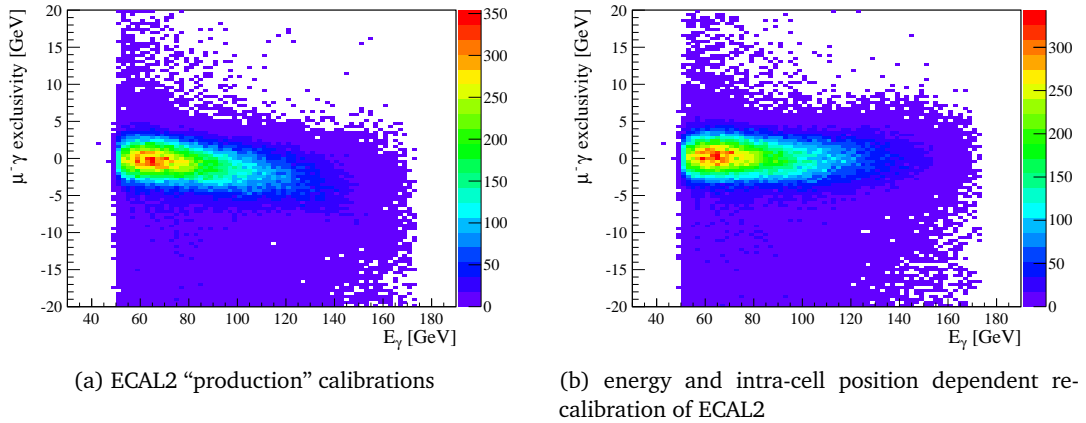
Figure 3.9: data: $\pi^-\gamma$ exclusivity against inferred photon energy

3.3 ECAL2 in the simulation
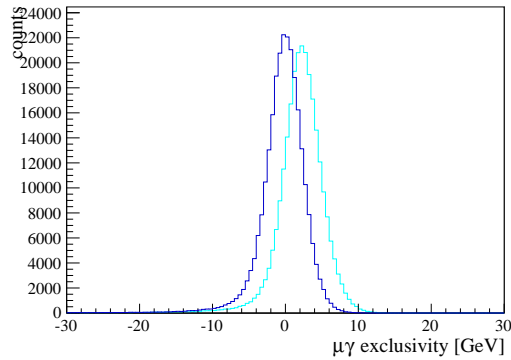
Figure 3.10: energy balance of simulated $\mu^-\gamma^* \to \mu^-\gamma$ events with default calibration (cyan) and after linear re-calibration (blue)

The reconstruction of shower energies from simulated data suffers from an energy-dependent bias as well. For the analysis on hand, the bias was approximated as a linear function of photon energy and corrected, reducing the width of the exclusivity peak (cf. Figure 3.10) from $\sigma = 2.9\,\mathrm{GeV}$ to $2.7\,\mathrm{GeV}$ as determined by fit of a Gaussian.

3.4 Merging of proximal ECAL2 clusters

(a) hadron beam

(b) muon beam
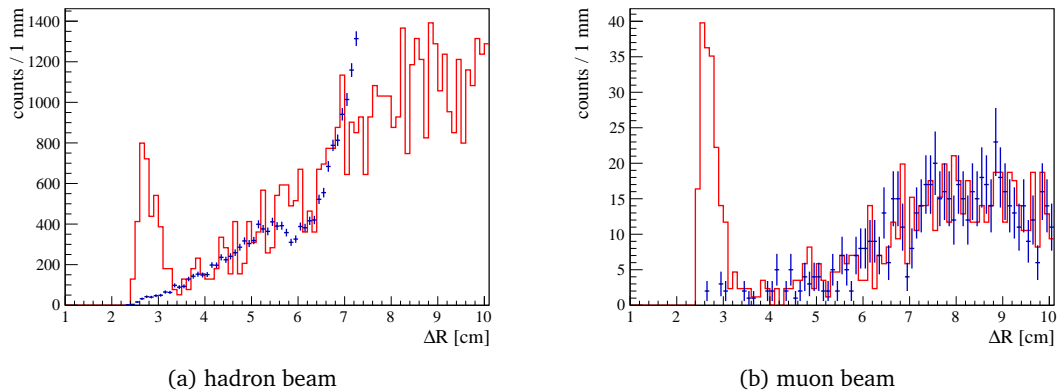
Figure 3.11: radial distance between the two highest-energetic showers reconstructed from ECAL2 (data and simulation)

After application of the calibrations described in the previous sections, another issue remains: The radial distance between the two ECAL2 showers with the highest energies in the simulation shows a peak around $3\,\mathrm{cm}$ which is absent from the data, as shown in Figure 3.11. This effect is interpreted as erroneous splitting of clusters by the shower fit

21

of CORAL and corrected by merging clusters whose radial distance is less than 3.5 cm in the analysis code.

3.5 Hadron beam energy determination from correlations of beam parameters

At the T6 primary target and the following collimators (cf. Section 2.1 for details of the COMPASS beams), the hadron beam particles are produced and selected with well defined correlations of their kinematic variables, which according to Liouville's theorem still must be intact, even after traversing more than 1 km of beam line. Following this observation and using charged 3-pion processes as a reference, a neural network was trained to make use of the four quantities X, Y, dX/dZ and dY/dZ (measured at $Z = -70$ cm) to determine the fifth parameter, the beam momentum [FK12].

While for the analysis at hand the full neural network[1] kindly provided by [Krä12] was employed, [Fri12a] also has obtained an approximation in polynomial form to avoid time-consuming neural network evaluations that is given in Appendix A.3.

3.6 BMS rescaling

Using calibrations for hadron beam momentum and ECAL2 energy as described above and measuring muon beam momentum via BMS, the energy scale is over-determined (three measurements for two types of beam). Since the BMS measurement is arguably the worst of the three[2] this inconsistency is resolved by shifting the BMS measurement down by a constant offset of 0.45 GeV.

3.7 Detector efficiencies used in simulation

Within this work, it has been found that the variation of the tracking efficiency with the momentum of the charged particle is not properly reproduced by the standard simulation setup, at least for small track angles which are typical for the Primakoff reactions. This effect is linked to deficits in the description of detector efficiencies in the simulation.

Figure 3.12 shows that in the kinematic domain of Primakoff-Compton scattering indicated by dashed red lines, pseudo-efficiencies obtained from simulation differ significantly from those observed in the data. Detectors whose efficiencies are described correctly are indicated by shades of green, whereas detectors and kinematic regions for which efficiency assumptions in simulation are too optimistic are coloured in shades of light and darker blue. In the extreme case of ST05U1db and ST05U1ub, a difference of nearly 100 % can be observed which is due to dead channels which cover almost the complete kinematic region of interest. For many detectors, the exhibited efficiency differences are momentum-dependent which is due to spatial efficiency variations which at the time of writing cannot be incorporated into the simulation due to a limitation of the implementation which assumes uniform efficiency across the whole detector plane.

---

[1]The source code will gladly be made available upon request to the author or to [Krä12].

[2]The BMS reconstruction code used in CORAL had not been calibrated very recently.
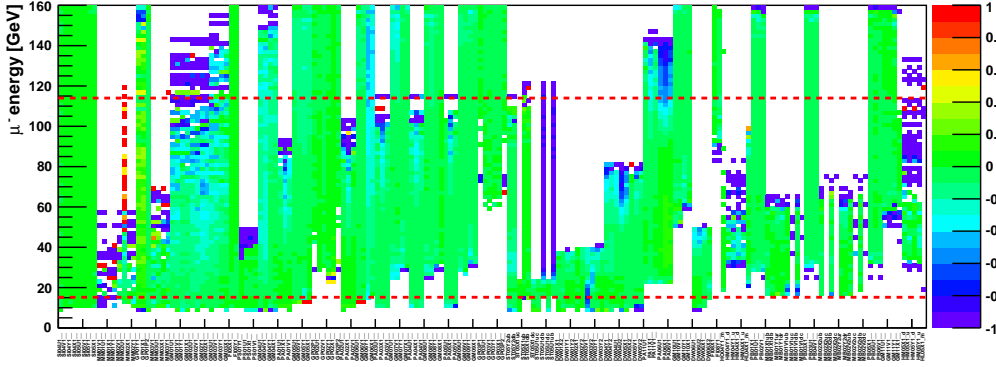
Figure 3.12: Depending on muon momentum (ordinate) and detector plane (abscissa) the colour scale indicates the differences between pseudo-efficiencies $\epsilon_{\text{data}} - \epsilon_{\text{sim}}$ obtained from $\mu^- \gamma \to \mu^- \gamma$ data and simulation.

To improve the description of detector efficiencies while staying within the capabilities of the current software chain, the average value of the efficiency is re-calibrated for each detector plane which contributes more than marginally to the measurement. Yet, in the detector simulation the proper efficiency is called for, but only the pseudo-efficiency is readily accessible. While pseudo-efficiencies generally can give a reasonable impression of a detector's performance, they often to some degree depend on surrounding detectors and on details of the tracking procedure so that they cannot simply be used in place of the proper efficiencies.

However it is a reasonable assumption (or even requirement) that in a correct spectrometer simulation all detector planes shall exhibit the same pseudo-efficiencies as they do in the experiment. That implies that for every detector plane, the linear relation between the proper efficiency ε_{det} and the pseudo-efficiency ϵ_{det}

$$\varepsilon_{\text{det}} = \epsilon_{\text{det}} + c_{\text{det}} \tag{3.2}$$

must hold for data and simulation with the same value of c_{det}. This implies that the proper efficiency may be updated by adding the difference of pseudo-efficiencies:

$$\varepsilon'_{\text{det,sim}} = \varepsilon_{\text{det,sim}} + \Delta\epsilon_{\text{det}} \tag{3.3}$$

$$\Delta\epsilon_{\text{det}} = \Delta\varepsilon_{\text{det}} = \epsilon_{\text{det,data}} - \epsilon_{\text{det,sim}} = \varepsilon_{\text{det,data}} - \varepsilon_{\text{det,sim}} \tag{3.4}$$

To avoid biasing detector plane efficiencies towards regions of high statistics which might lead to a systematic effect on the polarizability measurement, the per-plane efficiencies have been computed as weighted averages of the efficiencies ϵ^p_{det} determined in independent momentum bins:

$$\epsilon_{\text{det}} = \frac{\sum\limits_{p} w^p_{\text{det}} \epsilon^p_{\text{det}}}{\sum\limits_{p} w^p_{\text{det}}} \tag{3.5}$$

The weight w_{det}^p is defined as the fraction of tracks of momentum p which are passing through the active area of the detector relative to all tracks of that momentum, whereas *all tracks* refers to the sample of identified Primakoff-Compton reactions, both in cases of data and simulation:

$$w_{\text{det}}^p \quad = \quad \frac{N_{\text{det}}^p}{N^p} \tag{3.6}$$

This definition is devised to give weight to a momentum bin according to the average contribution to the tracks of that momentum (i.e. average number of hits) that the fully efficient detector plane would be expected to make and thus is determined by the geometric acceptance of that detector with respect to the spatial distribution of the Primakoff-Compton tracks of that momentum in the spectrometer.
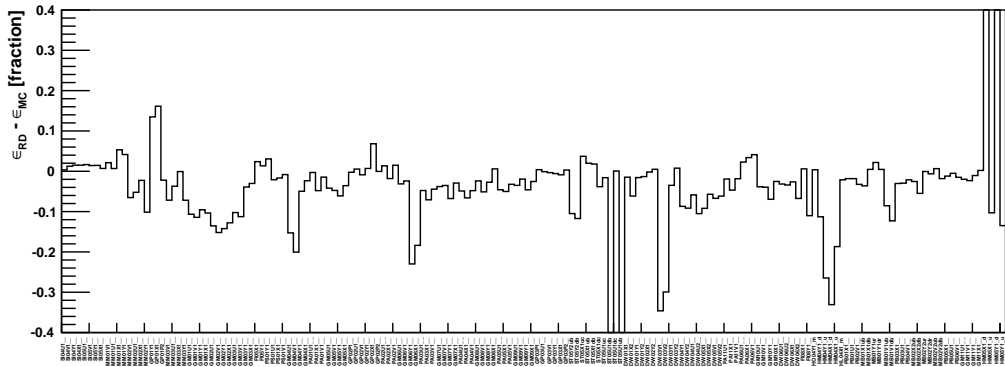

Figure 3.13: efficiency deviation (absolute numbers) between muon beam data and simulation with default efficiency settings

As demonstrated in Figure 3.13, with default efficiency settings, a large number of detectors show significant deviations between weighted efficiencies as obtained from data and from simulation. After adapting the efficiency inputs for the simulation, Figure 3.14 indicates that the situation is improved considerably. (Most of the remaining deviations now belong to detector planes which contribute so little to the measurement that they have been excluded from the calibration procedure.)

The described efficiency calibration has been performed independently for the data sets taken with the two different types of beam. Using an earlier, slightly different set of Primakoff cuts the impact on the extracted polarizability value was determined as $-0.8 \times 10^{-4}\,\text{fm}^3$ for muons and $-1.4 \times 10^{-4}\,\text{fm}^3$ for pions. It is assumed in this work that the calibration of the efficiency mean value eliminates the largest part of efficiency related errors, however it is to be expected that a residual effect remains due to spatial efficiency variations that cannot be replicated by the current simulation software. Following this consideration, the remaining systematic error is estimated to be $0.6 \times 10^{-4}\,\text{fm}^3$ which is a bit less than half of the absolute value of the effect of the efficiency calibration on the pion polarizability.
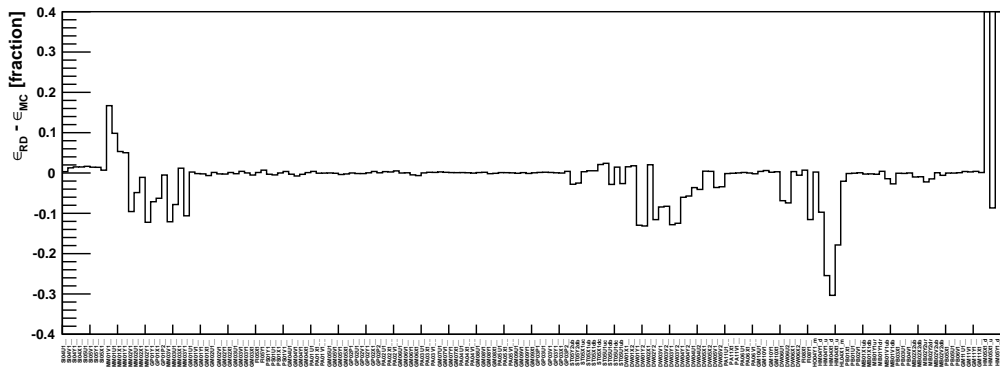
Figure 3.14: efficiency deviation (absolute numbers) between muon beam data and simulation after efficiency settings have been calibrated

Chapter 4

Event selection

4.1 Data quality

(a) hadron beam (b) muon beam
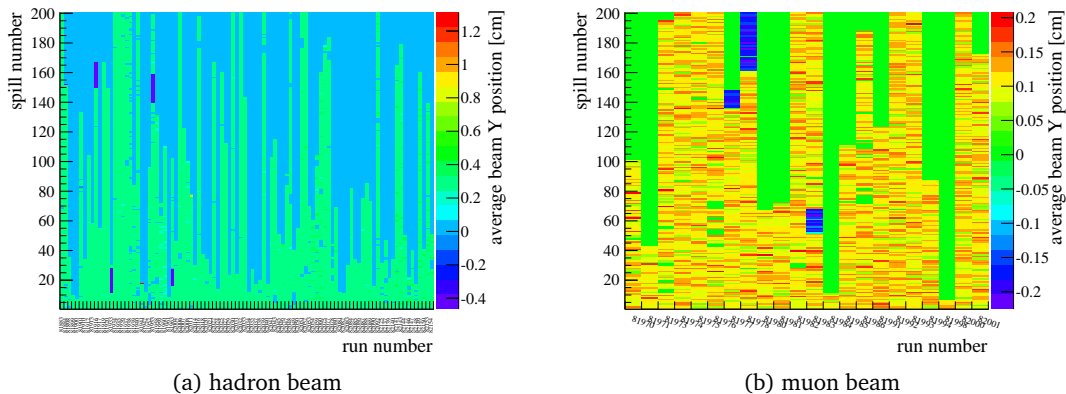
Figure 4.1: beam Y position, spills with beam line problems visible in dark blue

A variety of studies have been performed with the intent to identify errors during data recording such as abnormal beam conditions or detector malfunctions, a selection of which is mentioned here. Depending on the quantity studied and the statistics available the analysis was conducted at the level of *runs* or *spills* (cf. Section 2.7 for a definition).

The most frequent reasons for exclusion of spills were beam(line) instabilities (shown in Figure 4.1) and electronics problems that manifested themselves as jumps of the *TCS phase* (exhibited in Figure 4.2) which is the offset of the trigger time with respect to the last tick of clock of the trigger system running at 38.88 MHz. In the instance of two runs, erroneous ECAL2 calibrations have been identified (presented in Figure 4.3).

A list of spills to be excluded ("bad spill list" in COMPASS slang) has been compiled and made available to the collaboration by means of the COMPASS wiki [NG12].

Figure 4.2: TCS phase, spills with time jumps visible in red

Figure 4.3: energy balance of Primakoff-Compton scattering (run-wise normalization, muon beam)

4.2 Event topology

In accordance with the underlying physics process, events are selected which contain exactly one primary vertex with exactly one outgoing, negatively charged track and at least one shower in ECAL2 which has no charged track attached to it.
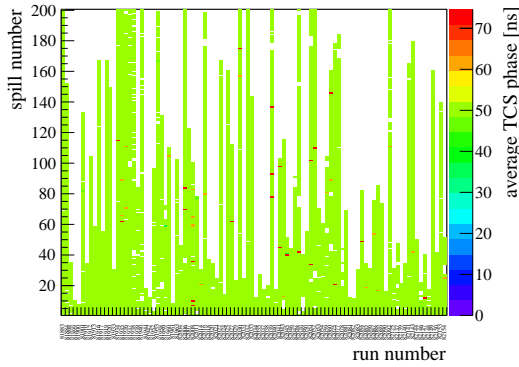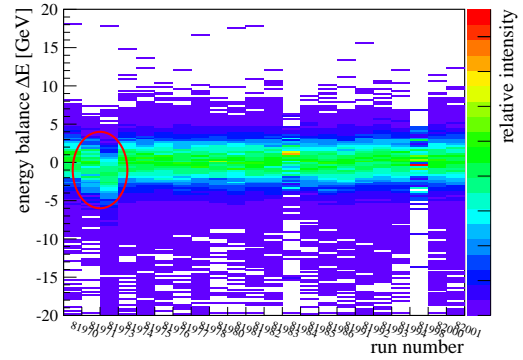
4.3 Trigger

For consistency reasons it is required that at least one of the Primakoff trigger was signalled and also that the event time was defined by one of the Primakoff triggers.

4.4 Recoil Proton Detector

As the scattered beam particle of Primakoff-Compton events is emitted at very forward angles, events in which a (large-angle) track in the Recoil Proton Detector (cf. Section 2.4 for a description) is registered are indicative of a different kind of interaction and thus are discarded. In that way, the RPD is used to connect to the angular range of the sandwich veto and to extend it towards larger angles.

4.5 Definition of beam kinematics and beam PID

The incoming beam is required to pass through the trigger elements of the alternative beam trigger aBT (cf. Section 2.6) which aims to ensure that the trigger was activated by the interaction at hand. Additionally, the beam divergence is subjected to an elliptic cut in dX/dZ and dY/dZ. The combination of these two cuts guarantees that the beam particle is passing well inside the dimensions of the target disc.

Further on, these restrictions to the beam parameters serve the important purpose of improving the quality of the beam: A substantial amount of μ^- background stemming from $K^- \to \mu^- \bar{\nu}_\mu$ decays is removed since the K^- decay momentum leads to an
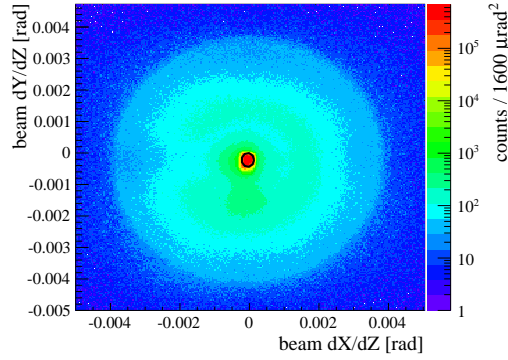
Figure 4.4: two-dimensional display of the divergence of the hadron beam (only pre-selection cuts applied, position of divergence cut indicated in black)

elevated average divergence of the (tertiary) μ^- beam particles compared to the (secondary) hadron beam. Plotting beam dY/dZ against dX/dZ in Figure 4.4 to support this presumption, a circle is visible at a radial divergence dR/dZ of ~ 3.85 mrad which corresponds very well to the kinematic cutoff at ~ 3.9 mrad that can been obtained from simulation of the $K^- \to \pi^- \pi^0$ decay. (Simulation of the $K^- \to \mu^- \bar{\nu}_\mu$ decay yields slightly larger divergences, however due to the low mass of the neutrino the shape of dR/dZ lacks a feature as readily identifiable as the kinematic cutoff of the decay into two pions.) Lastly, the beam cuts serve to reject beam particles that have undergone interactions in air or in beam line elements before passing through the target and thus help to clean up undesired events from the sample.

(a) before CEDAR cut

(b) after CEDAR cut
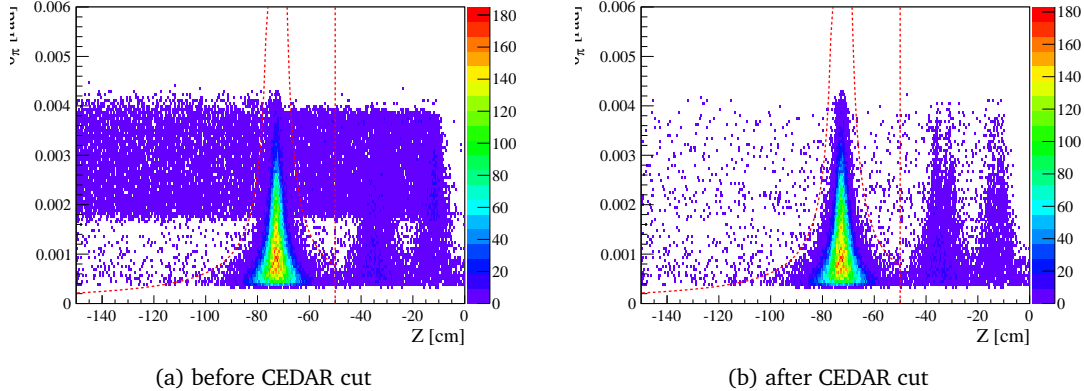
Figure 4.5: Reconstructed π^- scattering angle θ_π plotted against primary vertex Z position. The white band at scattering angles below ~ 0.6 mrad is a consequence of the p_T cut, whereas the cut in $m_{\pi\gamma}$ accounts for the lack of events with scattering angles above ~ 4.5 mrad.

To avoid the interpretation of interactions of the kaon beam contaminations (cf. Section 2.1 for details) as pion events, the identification of the beam particle as pion is

required in the CEDARs (cf. Section 2.3 for their description). The benefit of π^- ID is showcased in the distribution of reconstructed π^- scattering angle against primary vertex Z position which contains a sizable contribution of $K^- \to \pi^- \pi^0$ decays of beam kaons misidentified as Primakoff-Compton scattering, displayed side by side before and after CEDAR cut in Figure 4.5. The left plot shows a broad band of kaon decays with scattering angles between 2 and 4 mrad which are entering the Primakoff sample when one of the π^0 decay photons is low-energetic enough so that the π^- and the other, high-energetic photon pass the $\pi\gamma$ exclusivity cut. After application of the CEDAR cut, the right image reveals that the beam kaons are suppressed to a large extent. A quantitative evaluation of the effectivity is undertaken in Section 6.2.

To identify the pions in the hadron beam, the likelihood method developed in [Fri10] has been employed.[1] By analyzing the hit information of the individual PMTs with a likelihood approach instead of regarding PMT hit counts as in [Jas12], the performance is improved significantly as the need for extreme beam parallelity is overcome. The approach allows positive identification of the beam particle as pion and thus the rejection of kaons and anti-protons from the beam. Owing to their similarity in mass, muons cannot be separated from the pions in this way, but the scattered muons are identifiable by other means as described in Section 4.10. The suppression of beam electrons in the CEDARs has not been studied as electron bremsstrahlung events are removed by the cut on transverse momentum, anyways.

4.6   Primary vertex

As the experimental resolution of the primary vertex Z position strongly depends on the scattering angle θ of the beam particle (cf. Figure 4.5b), a θ-dependent Z cut is utilized to confine the interaction to the nickel target at $Z = -72.5$ cm. In addition, a constant cut at $Z = -50$ cm serves to avoid the tail of the vertex distribution that stems from interactions in one of the tungsten targets around $Z = -35$ cm.

4.7   Momentum transfer

The cut in q^2 is a defining step in the event selection as it acts to separate the electromagnetic interactions which are dominant at very low q^2, corresponding to large distances to the nucleus, from strong processes which happen much more frequently, but predominantly at larger q^2. The distributions of q and q^2 in the cut region are presented in Figure 4.6.

---

[1]Due to missing calibrations and missing correction for read-out errors [Fis12] an inefficiency of 22 % had been incurred on previous iterations of the CEDAR reconstruction code which by now has been resolved owing to work by [Gen11] and [Hub12].
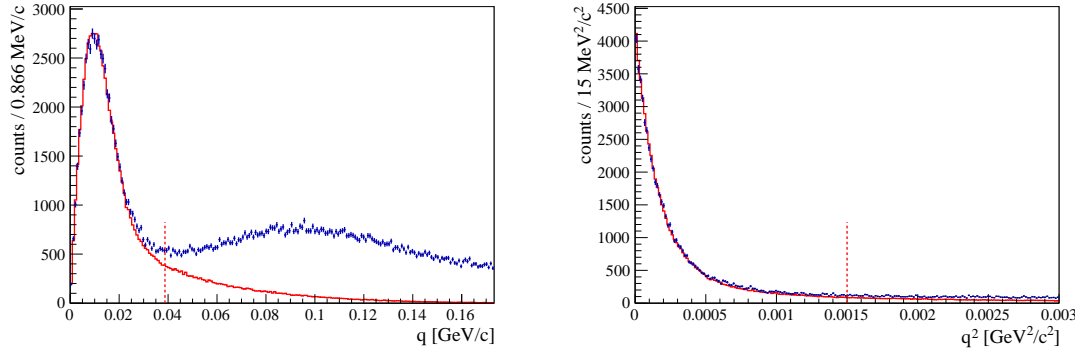
(a) The wide distribution around $q = 0.1\,\text{GeV}/c$ stems from background processes (mostly strong interaction).

(b) Fit with exponential plus second order polynomial yields an exponential slope of -6000 ± 300 as a measure of the experimental resolution.

Figure 4.6: $\pi^-\gamma$ momentum transfer to the nucleus

4.8 Final state mass

To avoid the background of $\rho^- \to \pi^-\pi^0$ decays from rho produced diffractively or electromagnetically, only events with low $m_{\pi\gamma}$ are accepted for analysis (cf. Figure 4.7). Nevertheless, a certain amount of this π^0 background stays with the data, the subtraction of which takes place at a later stage of the analysis and is elaborated in Section 7.3.
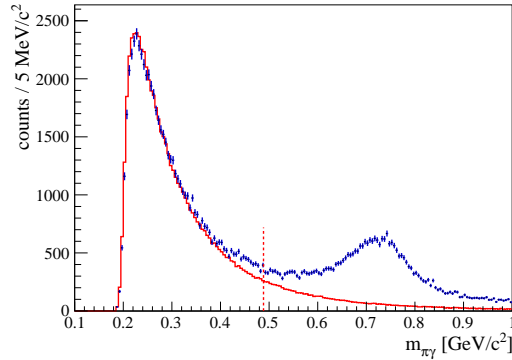
Figure 4.7: final state mass, π^0 background not subtracted

4.9 Transverse momentum

The cut on the transverse momentum p_T of the scattered pion serves the purposes of enforcing a well-defined primary vertex and suppressing events in which pions that have undergone multiple scattering pick up random clusters from ECAL2 (cf. Figure 4.8). Electron induced bremsstrahlung events stemming from the electron contamination of the beam are removed as well.
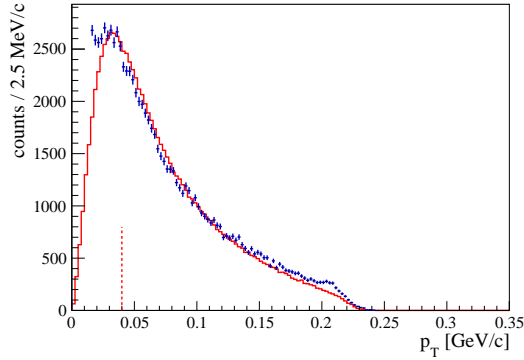
Figure 4.8: Transverse momentum of scattered pion. Around 0.21 GeV/c a small contribution of $\pi^- e^-$ scattering is visible, cf. Section 7.1. The distribution is cut around 0.22 GeV/c due the indirect effect of the cut on the final state mass.

4.10 Muon identification

As efficient identification of beam muons in the CEDARs is impossible[2], an alternative approach is chosen and scattered muons are rejected in the muon system of COMPASS in which they are discerned due to their capability of traversing large amounts of material without major loss in energy.
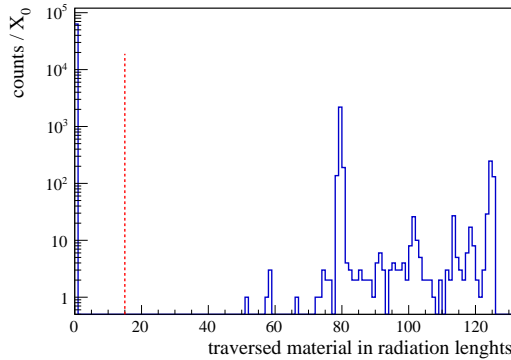
Figure 4.9: Area density measured in radiation lengths that is traversed by scattered pions. (Note the peak at zero.)
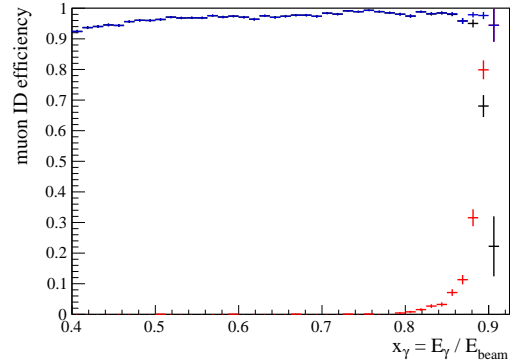
Figure 4.10: The dependency of the muon identification efficiency on x_γ is determined with muon beam data: The standard identification using CORAL is drawn in black, the special HO04 association in red and their combination in blue.

In practical terms this is accomplished by cutting on the amount of material that the scattered track has passed through, measured in units of radiation length X_0, the distribution of which is shown in Figure 4.9. For reasons currently not understood [Bed], the

---

[2]This holds true at least for the current experimental setup and the currently employed reconstruction method.

HO04 hodoscope which is used to identify muons that have passed through the calorimeters and the muon filter (a concrete wall) of the second spectrometer stage is not properly associated with charged tracks in the CORAL reconstruction software, leading to traversed material readings for these tracks which are artificially low. To compensate for this imperfection, a corrected HO04 association is performed at the level of the Primakoff analysis code. In that way, the geometric acceptance of HO04 is expanded considerably as shown in Figure 4.11. The effect on the muon identification efficiency is highlighted in Figure 4.10. Precisely at large x_γ where the fraction of muon background is highest due to muon spin induced enlarging of the cross section compared to the pion case, the CORAL identification efficiency drops off and is supplemented by the custom HO04 code.

(a) standard association in CORAL

(b) special association code
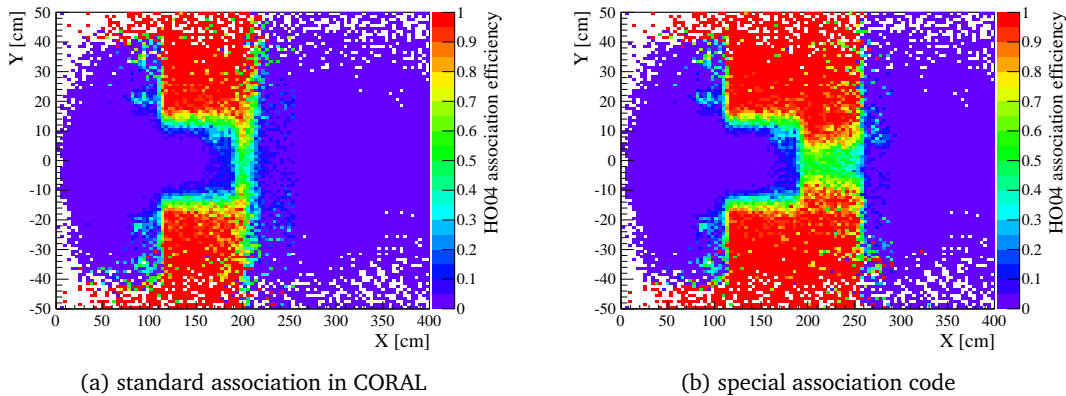
Figure 4.11: efficiency of association of the HO04 hodoscope to scattered muons depending on the position of the muon track at the Z of HO04 (only pre-selection cuts applied)

4.11 Energy balance

To ascertain exclusivity of the targeted reaction, a cut of $\pm 15\,\text{GeV}$ is placed on the energy balance (cf. Figure 4.12). After the extensive ECAL2 calibrations described in Section 3.2, an overall energy resolution of $\sigma_{\text{RD}} = 2.3\,\text{GeV}$ is attained (determined by fitting a Gaussian to the energy balance).

4.12 List of cuts

Summaries of the cuts that are applied to hadron and muon beam data are given in Table 4.1 and Table 4.2, respectively. The *events* column holds a running count of events which is reduced successively as cuts are applied in the given order. Cut strength expressed as reduction factor is specified in the *red. factor* column. And as a measure that is independent of the ordering of cuts, the *effect* column holds the reduction factor of the cut that would be effected if it was applied at the very end, after all other cuts have been taken. For the sake of clarity, cuts affecting less than 50 ppm of events have been omitted.
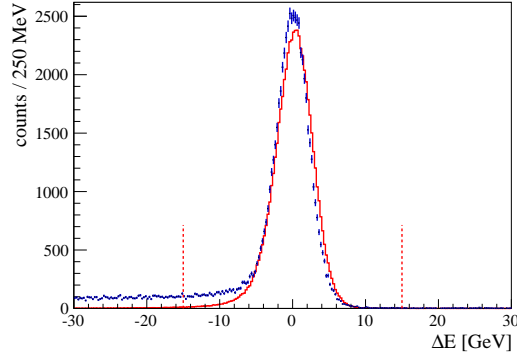
Figure 4.12: energy balance of $\pi^-\gamma^* \to \pi^-\gamma$

Variables used in the tables are defined as follows: E_γ is the energy of the ECAL2 cluster with highest energy. The radial extension of the beam R_{beam} is given as

$$R_{\text{beam}} = \sqrt{(X_{\text{beam}} - X_{\text{BC}})^2 + (Y_{\text{beam}} - Y_{\text{BC}})^2} \tag{4.1}$$

where X_{beam} and Y_{beam} are determined at the position of the Beam Counter ($Z = -670\,\text{cm}$) and defined relative to the centre of the Beam Counter which has been determined to lie at $(X_{\text{BC}}, Y_{\text{BC}}) = (0.7\,\text{mm}, 1.0\,\text{mm})$. In analogy, the radial beam divergence dR/dZ is defined as

$$\frac{dR}{dZ} = \sqrt{\left(\frac{dX - dX_0}{dZ}\right)^2 + \left(\frac{dY - dY_0}{dZ}\right)^2} \tag{4.2}$$

dX_0/dZ and dY_0/dZ being the centre of the pion beam angular distribution with $dX_0/dZ = -46\,\mu\text{rad}$ and $dY_0/dZ = -220\,\mu\text{rad}$.

cut	red. factor	events	effect
after pre-selection:		38175801	
exactly 1 primary vertex (PV)			
-300 cm $< Z_{\mathrm{PV}} <$ 50 cm			
PV: exactly 1 incoming charged track			
PV: exactly 1 outgoing neg. charged track			
$|\vec{p}_\pi| < 170$ GeV			
$E_\gamma > 50$ GeV			
bad spill list	0.9532	36390505	0.9566
Prim1 or Prim2 in trigger mask	0.9987	36343314	1.0000
Prim1 or Prim2 in main time mask	0.9994	36319932	0.9995
only 1 vertex associated with charged track	0.9886	35905041	0.9987
no recoil track in RPD	0.9716	34883802	0.9870
2 well-defined space points in SI after target	0.8956	31241123	0.9941
beam divergence $dR/dZ \lesssim 0.2$ mrad (elliptic)	0.8055	25163766	0.8953
beam counter: $R_{\mathrm{beam}} < 1.5$ cm	0.9018	22693578	0.9141
CEDAR π ID	0.9345	21207861	0.9382
θ-dependent Z-cut	0.7142	15146671	0.8475
$x_\gamma > 0.4$	0.4109	6224332	0.5590
$|t_{\mathrm{ECAL2}} - t_{\mathrm{track}}| < 6$ ns	0.9777	6085563	0.9972
$m_{\pi\gamma} < 3.5\, m_\pi$	0.6073	3695850	0.6221
$p_T > 40$ MeV/c	0.2705	999698	0.4877
$q^2 < 0.0015$ GeV^2/c^2	0.0795	79427	0.2616
π^- ID: $X/X_0 < 15$	0.9547	75831	0.9529
μ rejection: manual HO04 association	0.9992	75772	0.9993
exclusivity: $|E_\pi + E_\gamma - E_{\mathrm{beam}}| < 15$ GeV	0.8330	63115	0.8330

Table 4.1: list of cuts for the selection of the $\pi^-\gamma$ final state

cut	red. factor	events	effect
after pre-selection:		1850897	
exactly 1 primary vertex (PV)			
-300 cm < Z_{PV} < 50 cm			
PV: exactly 1 incoming charged track			
PV: exactly 1 outgoing neg. charged track			
$|\vec{p}_\mu| < 170\,\mathrm{GeV}$			
$E_\gamma > 50\,\mathrm{GeV}$			
energy balance: $|E_\pi + E_\gamma - E_{\mathrm{beam}}| < 50\,\mathrm{GeV}$			
bad spill list	0.8328	1541490	0.8492
Prim1 or Prim2 in trigger mask	0.9995	1540746	1.0000
Prim1 or Prim2 in main time mask	0.9997	1540325	0.9999
only 1 vertex associated with charged track	0.9965	1534860	0.9998
no recoil track in RPD	0.9847	1511422	0.9879
2 well-defined space points in SI after target	0.9520	1438879	0.9957
BMS likelihood > 0.02	0.7285	1048199	0.9393
beam divergence $dR/dZ \lesssim 0.6$ mrad (elliptic)	0.5331	558766	0.5403
beam counter: $R_{\mathrm{beam}} < 1.5$ cm	0.8338	465896	0.8346
θ-dependent Z-cut	0.7928	369378	0.8667
$x_\gamma > 0.4$	0.5009	185014	0.5949
$|t_{\mathrm{ECAL2}} - t_{\mathrm{track}}| < 6\,\mathrm{ns}$	0.9994	184898	1.0000
$m_{\mu\gamma} < 3.5\,m_\mu$	0.8433	155933	0.7649
$p_T > 40\,\mathrm{MeV}/c$	0.4910	76558	0.5237
$q^2 < 0.0015\,\mathrm{GeV}^2/c^2$	0.8148	62381	0.8454
exclusivity: $|E_\mu + E_\gamma - E_{\mathrm{beam}}| < 15\,\mathrm{GeV}$	0.9795	61104	0.9795

Table 4.2: list of cuts for the selection of the $\mu^-\gamma$ final state

Chapter 5

Method of polarizability determination

5.1 Parameterization

As a detailed simulation of the pion-Compton scattering is required to correct for the acceptance of the COMPASS apparatus, it is convenient to obtain the pion polarizability α_π directly from the ratio R of data divided by the simulation of the Born cross section. To that end, the formulation of the differential cross section as a sum of a Born term and a polarization term

$$\frac{d\sigma}{dE_\gamma} = \frac{d\sigma_{\text{Born}}}{dE_\gamma} + \frac{d\sigma_{\text{pol}}}{dE_\gamma} \tag{5.1}$$

from [GM80], based on the assumption of $\alpha_\pi + \beta_\pi = 0$ and with q_{min}^2 and q_{max}^2 denoting the kinematic limits of the momentum transfer to the nucleus, is employed:

$$\frac{d\sigma}{dE_\gamma} = \underbrace{\frac{4Z^2\alpha_{\text{em}}^3 E_\pi}{m_\pi^2 E_\gamma E_{\text{beam}}} \left[\frac{2}{3} \ln \frac{q_{\text{max}}^2}{q_{\text{min}}^2} - \frac{19}{9} + 4\sqrt{\frac{q_{\text{min}}^2}{q_{\text{max}}^2}} \right]}_{\text{Born cross section}} - \underbrace{\frac{4Z^2\alpha_{\text{em}}^2 \alpha_\pi m_\pi E_\gamma}{E_{\text{beam}}^2} \left[\ln \frac{q_{\text{max}}^2}{q_{\text{min}}^2} - 3 + 4\sqrt{\frac{q_{\text{min}}^2}{q_{\text{max}}^2}} \right]}_{\text{pion polarization term}} \tag{5.2}$$

Approximating 19/9 by 2 and neglecting the root terms which are small compared to the logarithms, the following compact formula is obtained for the ratio R which only depends on the kinematic variable $x_\gamma = E_\gamma/E_{\text{beam}}$:

$$R(x_\gamma) = \frac{\frac{d\sigma_{\text{Born}}}{dE_\gamma} + \frac{d\sigma_{\text{pol}}}{dE_\gamma}}{\frac{d\sigma_{\text{Born}}}{dE_\gamma}} = 1 + \frac{3}{2} \frac{\alpha_\pi m_\pi^3 x_\gamma}{\alpha_{\text{em}}(1 - x_\gamma)} \tag{5.3}$$

The value and error of the pion polarizability thus is obtained from the numerical fit of $c\,R(x_\gamma)$ (with nuisance parameter c) to the experimental ratio

$$R_{\text{exp}}(x_\gamma) = \frac{N_{\text{data}}(x_\gamma)}{N_{\text{sim}}(x_\gamma)} \tag{5.4}$$

which is determined from the event counts $N(x_\gamma)$ of experimental data and simulation in bins of x_γ.

5.2   Generator

The heart of the Primakoff generator consists of calculations of the $\pi\gamma^* \to \pi\gamma$ and $\mu\gamma^* \to \mu\gamma$ differential cross sections by Norbert Kaiser which include the polarizability contribution, first order Compton vertex corrections and soft photon emission. For pions also 1-loop contributions are included. A detailed description of these calculations and their numerical evaluation is given in [Fri12b], Chapter 2.5. For the purpose of employing the calculations in the event generator of the simulation chain, the polarizability contributions are set to zero and the differential cross sections are evaluated using a sample-and-reject method.[1]

In the following, some of the corrections to the pure Born cross section (which in their entirety sometimes sloppily are referred to as "radiative corrections") will be discussed in greater detail for the kinematic domain selected for the present analysis (cf. Table 4.1 for the list of cuts). The effect of the pion loop has been prepared in Figure 5.1 by dividing 10^8 events generated for Born cross section with loop contributions by the same number of events produced with pure Born cross section at the generator level. This method does not preserve the relative normalization of the different calculations but it allows a rough estimation of the effect on the polarizability result by fitting the ratio with Eq. (5.3).
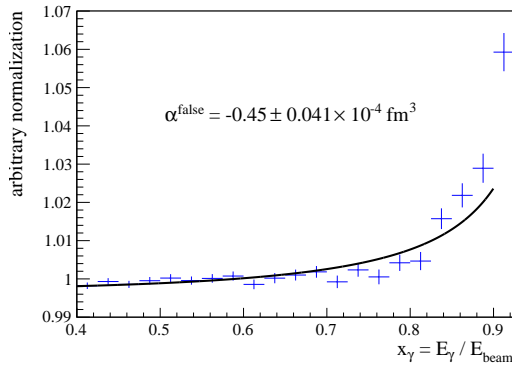

$$\alpha^{\text{false}} = -0.45 \pm 0.041 \times 10^{-4}\ \text{fm}^3$$

Figure 5.1: Born with pion loop over Born (pion)

5.2.1   Compton vertex correction

The cumulative effects of pion loop and Compton vertex corrections and soft photon emission are shown in Figure 5.2 which is generated in full analogy to Figure 5.1 and displays the ratio of a 10^8 generator event sample of Born cross section with Compton and soft photon corrections and (for pions) loop contribution divided by a pure Born sample of identical size.

---

[1]The source code of the generator will gladly be made available upon request to the author or to [Fri12a].
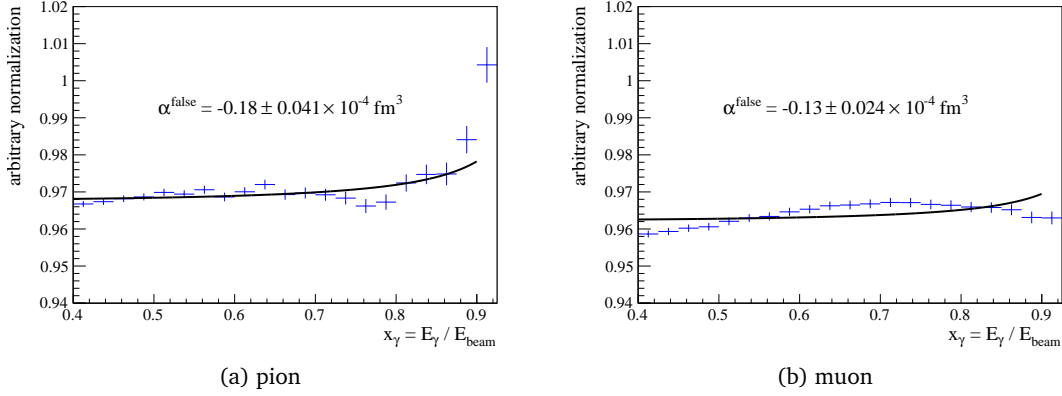
Figure 5.2: Born cross section with Compton and soft photon corrections and (for pions) loop contribution divided by pure Born cross section

5.2.2 Nuclear form factor

For the form factor of the Ni nucleus the Fourier transformation of a uniform sphere according to [Hof56] is employed using the measurement of the nickel radius r in [VJV87]:

$$F(|\vec{q}|) = \frac{\sin |\vec{q}|r - |\vec{q}|r \cos |\vec{q}|r}{|\vec{q}|^3 r^3} \tag{5.5}$$

The cumulative effects of pion loop, Compton vertex corrections, soft photon emission and nuclear form factor compared to the pure Born cross section are shown in Figure 5.3.
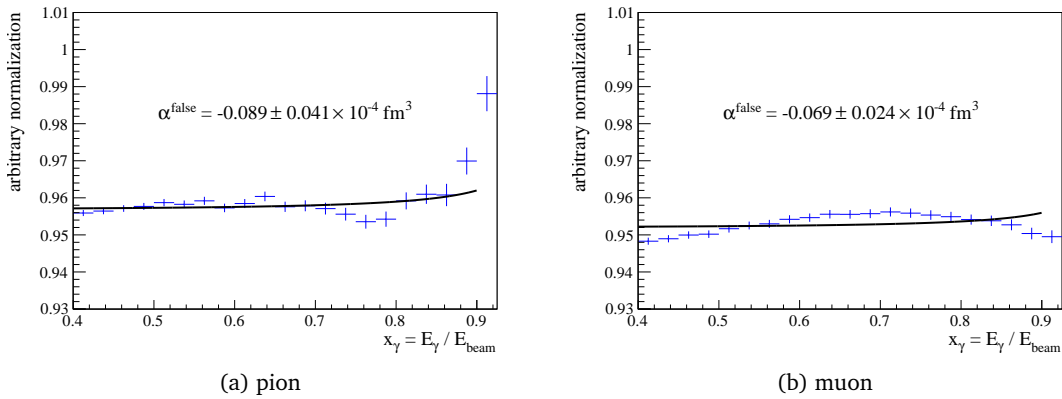
Figure 5.3: Born cross section with Compton and soft photon corrections, (for pions) loop contribution and nuclear form factor applied, divided by pure Born cross section

5.2.3   Systematic error

Due to primitive treatment of the nuclear form factor and because of missing corrections for electron screening, vacuum polarization and multi-photon exchange, a systematic error of $0.3 \times 10^{-4}\,\mathrm{fm}^3$ is assumed for the corrections to the Born cross section.

Chapter 6

Systematic studies

6.1 Muon control measurement

A major benefit of the polarizability measurement at COMPASS compared to other experiments is the possibility to use muon beam for systematic studies. The reaction $\mu^- Z \to \mu^- \gamma Z$ is closely related to the pion process and allows extraction of a hypothetical muon polarizability with exactly the same methodology as for data with pion beam. Of course, with the well-founded understanding of the muon being a point-like particle, the result for the polarizability is expected to be zero which means that the ratio of real data over Monte Carlo must be compatible with a flat line, possible deviations of which would be pointing towards shortcomings in the analysis.
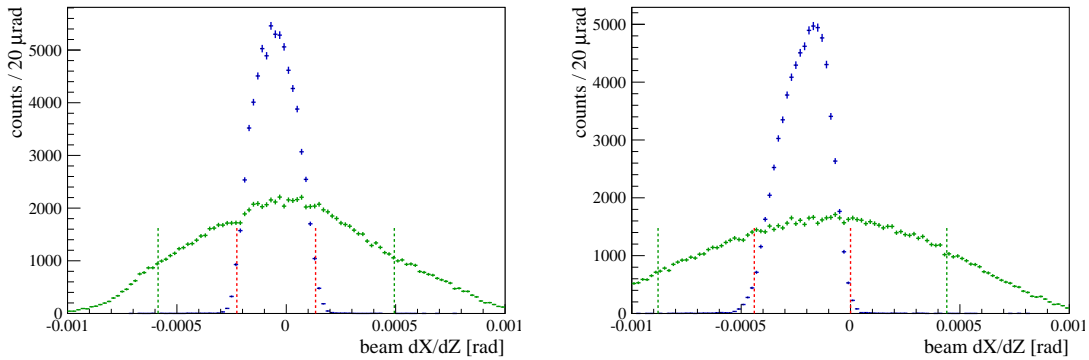
Figure 6.1: comparison of divergences of hadron (blue) and muon beam (green)

However, there is the caveat that the beam divergence of the muon beam exceeds that of the hadron beam by a large extent as visible in Figure 6.1 so that parts of the muon beam data are subject to different systematics than the hadron beam data. The low-angle tracking is very sensitive to variations of the track angles because of the transitions between different groups of tracking detectors covering different angular domains is taking place in that kinematic region. Also, the geometry of the light gas pipe of the COMPASS RICH detector has a considerable influence on low angle tracking efficiencies so that the difference in beam divergence may not be disregarded lightly.

As a consequence, the muon ratio is computed for two alternative configurations: In Figure 6.2a the complete data set is shown without reserve whereas in Figure 6.2b the radial muon beam divergence is restricted to approx. $\pm 0.6\,\text{mrad}$ which excludes extreme angles but still is three times larger than the kinematic region of the hadron beam data. (In Figure 6.1 the cuts on hadron beam data are indicated by red dashed lines and the cuts on the *restricted* set of muon beam data by green dashed lines.)

Fitting the ratios with Eq. (5.3) in the range $0.4 < x_\gamma < 0.9$ which is used for the extraction of the pion polarizability yields $\alpha_\mu^{\text{false}} = 0.58 \pm 0.38 \times 10^{-4}\,\text{fm}^3$ for the full muon statistics and $\alpha_\mu^{\text{false}} = 0.64 \pm 0.52 \times 10^{-4}\,\text{fm}^3$ in the case of the *restricted* muon beam kinematics.

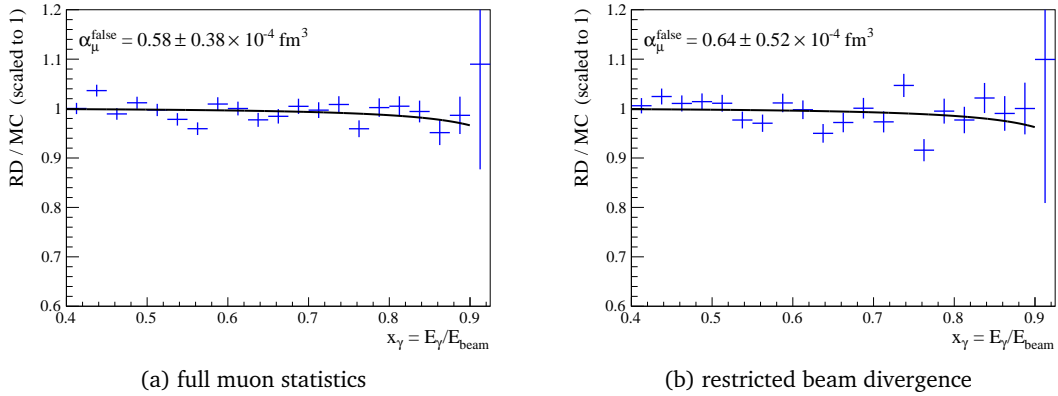(a) full muon statistics

(b) restricted beam divergence

Figure 6.2: muon beam data divided by simulation

Thus, the control measurement with *restricted* muon beam kinematics does not raise any doubt on the validity of the extraction of the pion polarizability, although the significance of this conclusion is limited due to the low level of accuracy achievable with the slim statistics of that data set.

The fit result from the full muon statistics might cautiously be interpreted as a systematic effect for data with high beam divergence (CL = 87%). Further insight may be gained by regarding the development of the result for the false polarizability depending on the beam divergence cut which is shown in Figure 6.3a and the different results obtained for different slices of beam divergence which is depicted in Figure 6.3b: There is an indication for a systematic effect at large beam divergences but not at the low divergence that are relevant for the analysis at hand.

6.2 K^- decays

The contribution of kaons to the hadron beam (cf. Section 2.1) allows a wide range of systematic studies, some of which are presented in this section. A sample of free $K^- \to \pi^- \pi^0$ decays of beam kaons is selected by reconstructing the exclusive $\pi^- \pi^0$ final state outside of the target with kaon selection in the CEDARs (cf. Section 4.5) and cut on low q^2 as the decay by definition is free of recoil. The kinematic cuts are indicated in Figures 6.4a, 6.4b, 6.5a and 6.6 revealing spectra that are virtually background-free. A slight mis-calibration
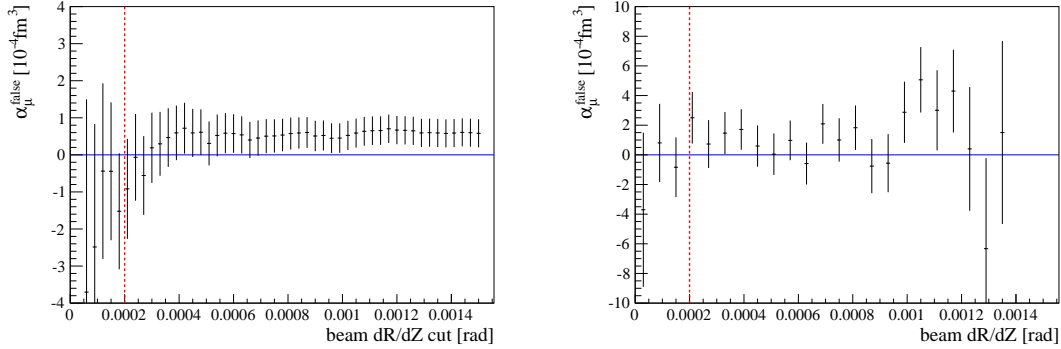
(a) false muon polarizability depending on beam divergence cut

(b) false muon polarizability obtained in slices of beam divergence

Figure 6.3: Studies of false muon polarizability: For comparison the cut on hadron beam divergence is indicated by the red dashed line.

of the ECAL2 energies in the simulation is visible as small shifts in the mass and energy balance plots and can be attributed to the fact that the simulated ECAL2 energies have been calibrated to with regard to the high photon energies that are used in the polarizability analysis at the expense of accuracy at low energies.
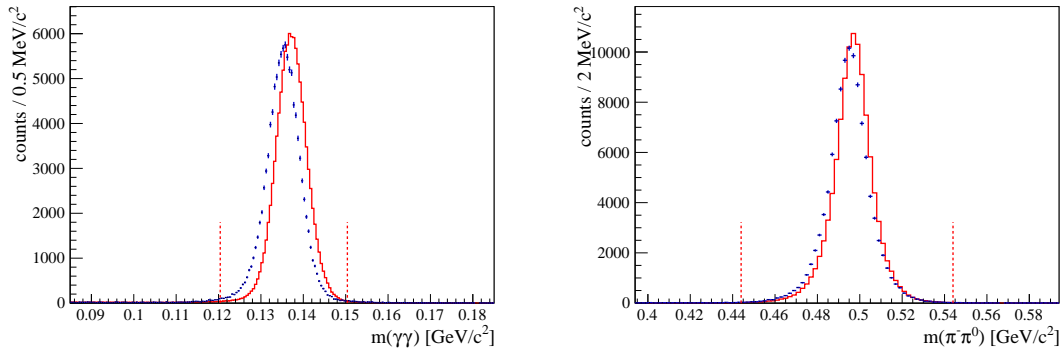
(a) combined mass of the event's two highest-energetic photons, Gaussian fit yields $\sigma = 3.8\,\mathrm{MeV}$

(b) combined mass of π^- and π^0, Gaussian fit to the center of the distribution yields $\sigma = 9\,\mathrm{MeV}$

Figure 6.4: free $K^- \to \pi^- \pi^0$ decays of beam kaons

The nickel target is seen as a prominent step in the distribution of vertex Z position in Figure 6.5b as the conversion of decay photons in the target decidedly reduces the π^0 reconstruction efficiency upstream of the target. The drop towards the position of SI03 is explained by the reduction in vertexing efficiency upstream of SI03. The two Z ranges upstream and downstream of the nickel target that are used for the decay sample are indicated in the plot.

As the momentum transfer of the K^- decay obviously is zero, its measurement allows the direct determination of the experimental resolution in q^2 as shown in Figure 6.6. The

(a) energy balance, $\sigma = 2.5\,\text{GeV}$ determined in Gaussian fit

(b) decay vertex Z position
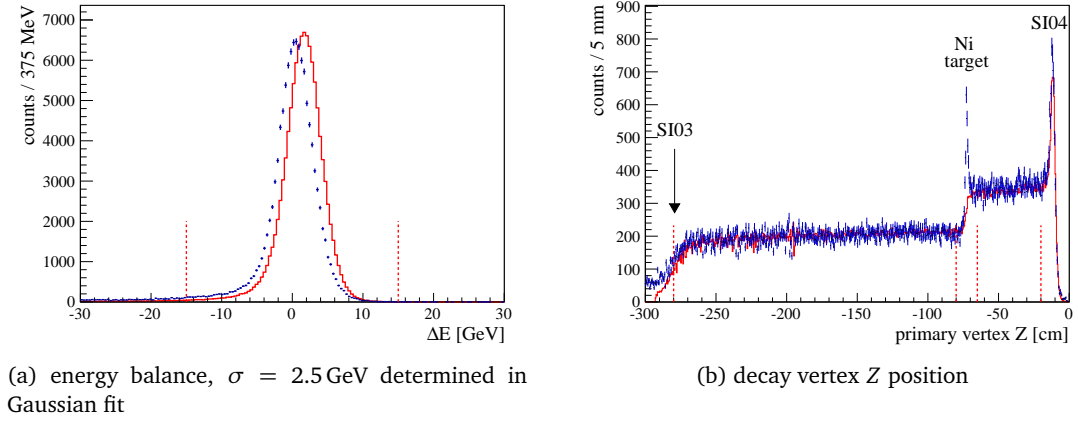
Figure 6.5: free $K^- \to \pi^- \pi^0$ decays of beam kaons

(a) experimental resolution in q^2: fit of double exponential yields a slope of $(9000 \pm 100)\,\text{GeV}^2/c^2$

(b) experimental resolution in q

Figure 6.6: free $K^- \to \pi^- \pi^0$ decays of beam kaons (data: blue, simulation: red)

agreement observed between data and simulation is remarkable.

Figure 6.7: $\pi^- \pi^0$ mass without CEDAR cut (blue) and with pion selection in the CEDARs (green)

Another interesting application of the K^- decay sample is the quantification of the CEDAR performance. In Figure 6.7 the final state mass is shown once without CEDAR cut and once with *pion* selection in the CEDARs. Taking the ratio of the number of events in the kaon peaks (obtain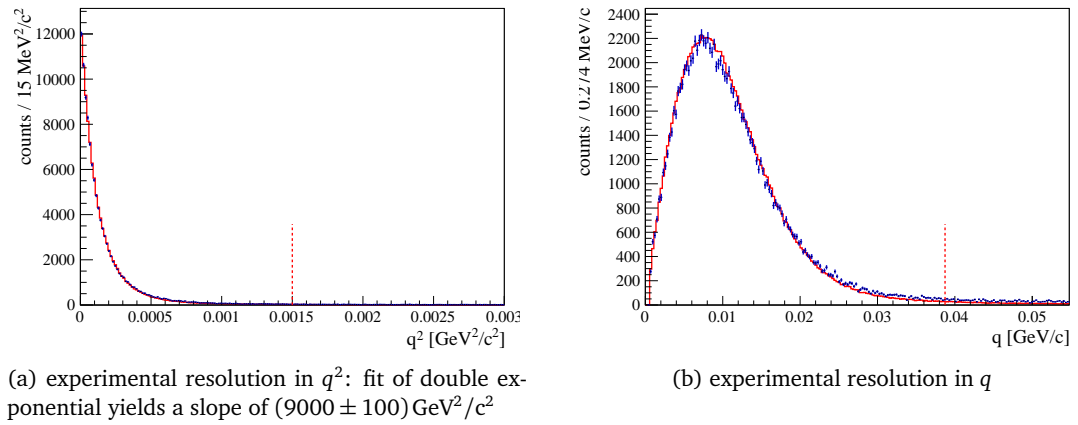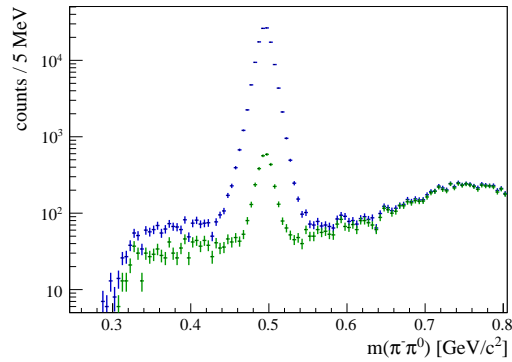ed by fit of Gaussians) of these two conditions, the *kaon suppression factor* of the CEDARs is measured as 50 ± 2 for the calibration by [Fri10].

(a) without CEDAR cut

(b) with kaon selection in the CEDARs
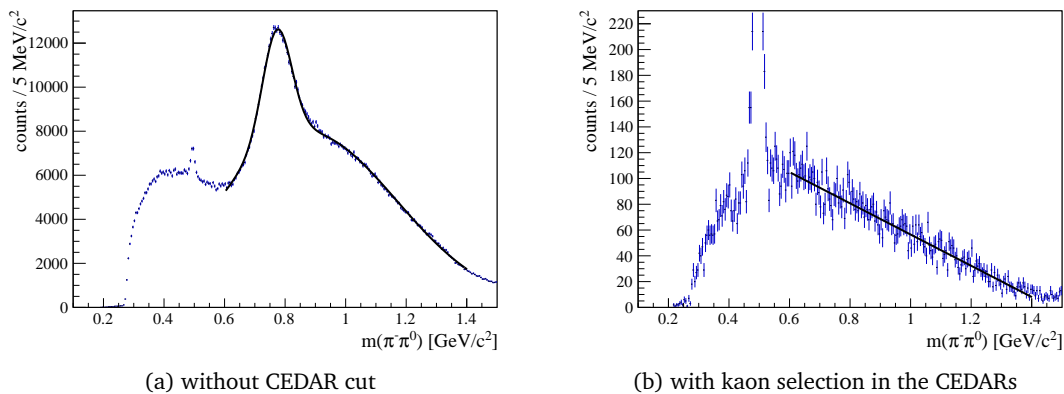
Figure 6.8: $\pi^- \pi^0$ mass for in-target events

The determination of the *pion suppression factor* is not as straightforward. To that end, the Z cut is inverted to obtain a sample of ρ^- from target interactions (Figure 6.8a) which is fitted with the sum of two Gaussians on top of linear background. After selecting CEDAR identified kaons, no visible trace of the ρ^- is left in Figure 6.8b. The visible impression is confirmed by the fit which yields zero pion events. In principle, the lower limit on the *pion suppression factor* could be inferred as 6000 from the random error of this zero result, however the systematics of the straight-line background is hard to estimate, so that this should not be taken at face value and rather be interpreted as indication of the order of magnitude.

A different use of beam kaon decays with a very tangible result is that of beam flux normalization (the kaon fraction of the beam is known to high precision from [ABD$^+$80]) which has been suggested by the author of this work in [NFP08] and which has been implemented in [A$^+$12].

To showcase the exciting physics potential of the beam kaons at COMPASS, the mass of the $K^-\pi^0$ final state is produced in Figure 6.9 in which $K^*(892)$ and $K_2^*(1430)$ clearly can be identified. For the latter, the mass $m = (1424 \pm 6)\,\text{MeV}$ and the full width $\Gamma = (98 \pm 23)\,\text{MeV}$ are determined from the fit of a non-relativistic Breit-Wigner resonance on top of quadratic background well in agreement with the world averages of the Particle Data Group [B$^+$12a]: $m_{\text{PDG}} = (1425.6 \pm 1.5)\,\text{MeV}$ and $\Gamma_{\text{PDG}} = (98.5 \pm 2.7)\,\text{MeV}$.
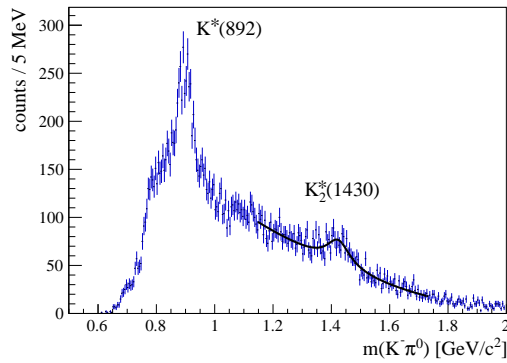

Figure 6.9: $K^-\pi^0$ mass for in-target events

Chapter 7

Treatment of backgrounds

Before the pion polarizability may be extracted, it is necessary to account for all of the underlying backgrounds. The suppression of the leptonic contribution to the beam is discussed for electrons in Section 4.9 and for muons in Section 4.10.

7.1 Pion electron scattering

A relevant source of background is pion electron scattering with subsequent electron bremsstrahlung $\pi^- e^- \rightarrow \pi^- e^- \rightarrow \pi^- e^- \gamma$ where enough of the electron energy is transferred to the radiated photon or photons (reconstructed as a single cluster in ECAL2) so that $\pi^- \gamma$ pass the exclusivity cut and where the electron track is not reconstructed or not attached to the primary vertex so that the event topology is the same as that of a $\pi^- Z \rightarrow \pi^- \gamma Z$ event.

Yet, it has been shown by [Gus11] that the statistics of the mis-identified process is very low and therefore the process may not add more than $0.2 \times 10^{-4}\,\mathrm{fm}^3$ to the systematic error of the polarizability measurement.

7.2 K^- decays

The decay of beam kaons into $\pi^- \pi^0$ (BR 21 %) is well suited to serve as an example of background that is to be expected from final states with one or several π^0. In the center of mass system of the π^0, decay photons are emitted back to back isotropically which gives rise to a flat $\cos\theta_{\mathrm{CMS}}$ distribution, with θ_{CMS} being the angle of the leading photon with respect to the direction of π^0 momentum. In case of very forward angles, almost the full energy of the π^0 is carried by the leading decay photon, whereas the sub-leading photon only takes a negligible amount. Consequently, when interpreted as a $\pi^- \gamma$ final state the energy balance of such events is almost exclusive. With larger θ_{CMS}, however, an increasing amount of energy is carried by the sub-leading photon, so that energy balance is getting progressively non-exclusive. As a consequence, in the plot of exclusivity against final state mass as shown in Figure 7.1a, the misidentified $K^- \rightarrow \pi^- \pi^0$ decays can be seen as a narrow vertical line with $\pi\gamma$ mass around 0.45 GeV, slightly below K^- mass. This interpretation of Figure 7.1a can be confirmed by re-producing the histogram with

(a) without CEDAR cut

(b) with CEDAR cut
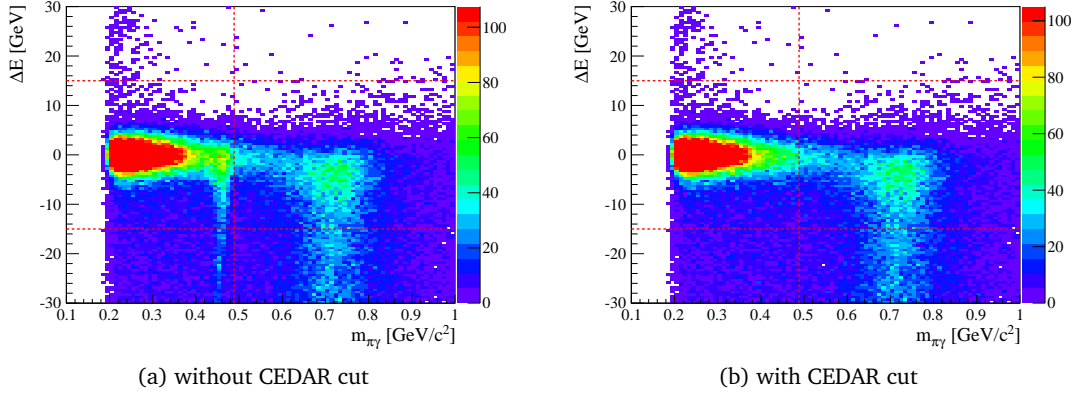
Figure 7.1: $\pi^- \to \pi^- \gamma$ energy balance vs. $m_{\pi\gamma}$ (hadron beam data, colour scale magnified to improve contrast)

CEDAR cut applied (cf. Section 4.5), removing all beam kaons: The specified structure disappears completely.

7.3 π^0 background

Besides kaon decay, further channels contribute to π^0 background. The exclusive π^0 production $\pi^- \gamma^* \to \pi^- \pi^0$ serves as another source and so does predominantly diffractive pion production $\pi^- \gamma^* \to \pi^- \pi^0 \pi^0$ which due to its high total cross section cannot be neglected, although the fraction of the phase space that passes Primakoff cuts is small. (In principle, final states with η could contribute to the background by exactly the same mechanism as those with π^0, however due to the generally much smaller cross sections in producing η, it has not been considered as a source of background.)

(a) energy balance, presuming $\pi^- \to \pi^- \gamma$

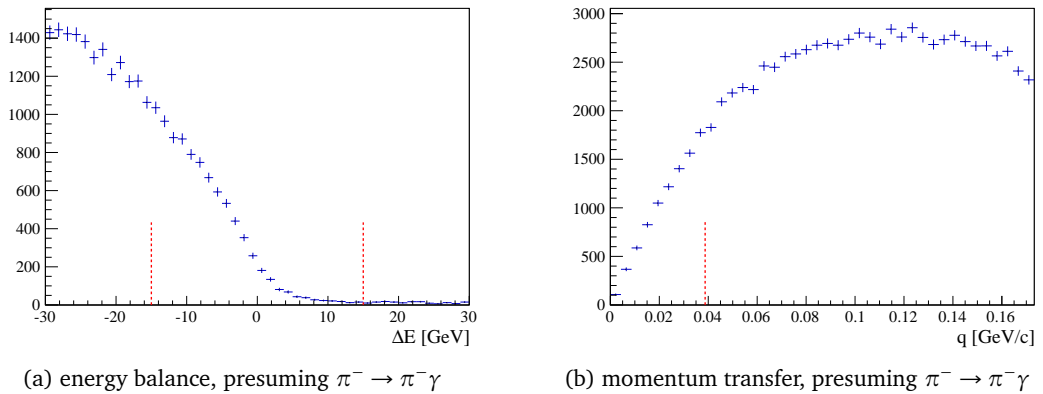(b) momentum transfer, presuming $\pi^- \to \pi^- \gamma$

Figure 7.2: simulated $\pi^- \pi^0$ background

To improve the understanding of backgrounds with π^0, a sample of $\pi^- \pi^0$ is simulated

based on hadron beam events from which an approximately symmetric π^0 decay could be identified in the $\gamma\gamma$ mass spectrum but for which energy conservation and small q^2 have not been required in order to create a sample with minimal bias. These events are replayed in the simulation with random π^0 decay angles to obtain unbiased $\pi^-\pi^0$ distributions, of which energy balance and q are presented in Figure 7.2. Naturally, the bulk of the simulated data lie outside the Primakoff cuts in both plots: π^0 background must vanish both for $\Delta E \to 0$ and for $q \to 0$ according to phase space considerations.

7.4 Strong background

(a) hadron beam data   (b) muon beam data
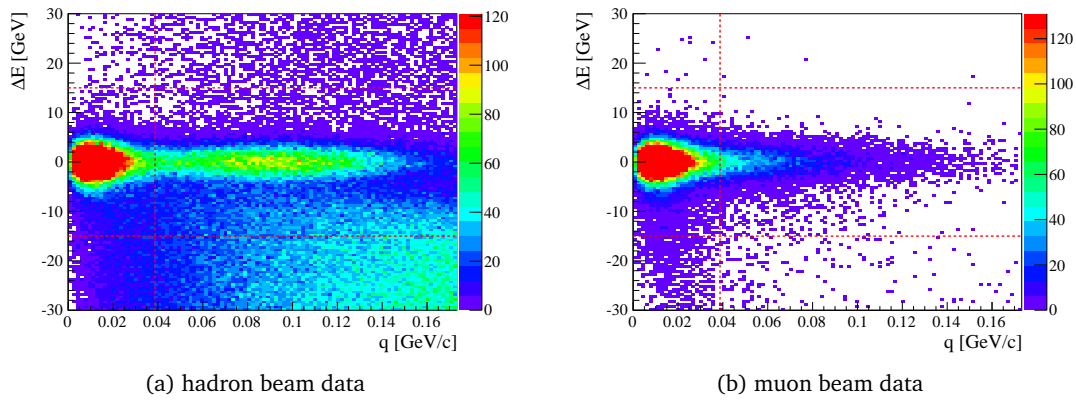
Figure 7.3: exclusivity vs. q (colour scale magnified)

(a) hadron beam data   (b) muon beam data
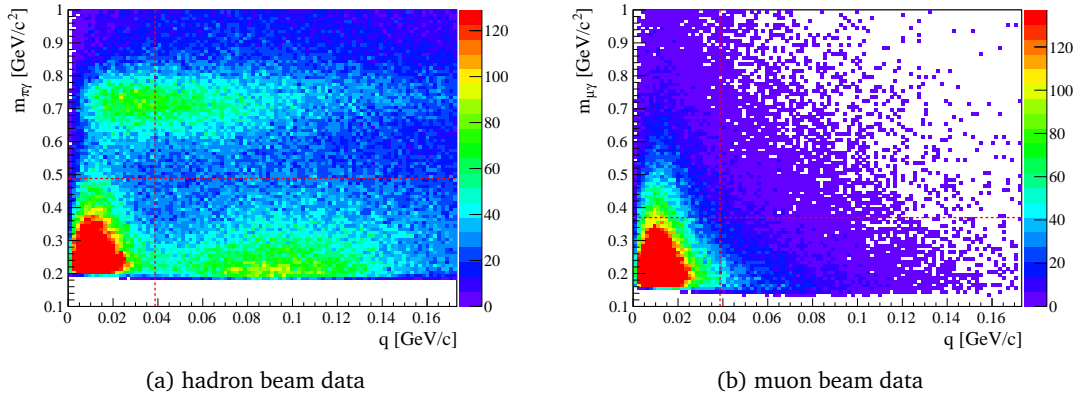
Figure 7.4: final state mass vs. q (colour scale magnified)

In addition to π^0 backgrounds characterized by non-exclusivity, there is a species of exclusive background as shown on Figure 7.3a around $q = 0.1\,\mathrm{GeV}/c$. The observations that it is centered around ΔE, does not appear on the corresponding plot from muon beam data (cf. Figure 7.3a) and exhibits similar x and s trends as the Primakoff events point

toward a $\pi^- Z \to \pi^- \gamma$ reaction mediated by the strong force as the source as depicted in Figure 7.5. The fact that this kind of background is different from π^0 backgrounds may also be inferred from Figure 7.4, which has both backgrounds showing up at very separate locations.
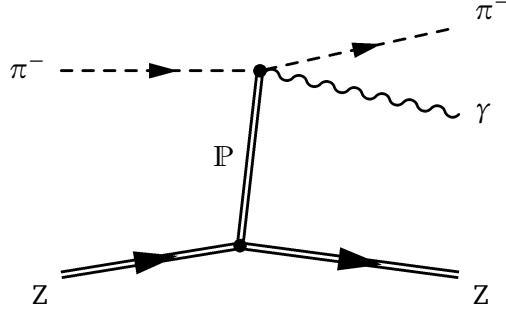

Figure 7.5: strong $\pi^- Z \to Z \pi^- \gamma$ process

7.5 Joint subtraction of π^0 and strong backgrounds

The unique q shapes of the Primakoff data and of the different background contributions allow the determination of the amount of background that lies beneath Primakoff events, within all kinematic cuts. To that end, for every x_γ bin, the q distribution is fitted with a model consisting of the sum of Primakoff signal, strong background and π^0 background using the log-likelihood method:

$$
\begin{aligned}
S(q) &= a_1 \, q^2 \, e^{-b_1 q} + a_2 \, e^{-b_2 q^2} & (7.1) \\
B_s(q) &= a_3 \, q^2 \, e^{-c q^2} & (7.2) \\
B_\pi(q) &= a_4 \, q \, e^{-d q} & (7.3) \\
M(q) &= S(q) + B_s(q) + B_\pi(q) & (7.4)
\end{aligned}
$$

Following the description of the cross section, the Primakoff signal $S(q)$ should adhere to a $q^2 e^{-b_1 q^2}$ form, however the addition of the $e^{-b_2 q^2}$ term is required due to the limited resolution of the experimental apparatus. Excellent agreement with the experimental shape was confirmed by comparison with $\mu^- \gamma$ simulation, $\pi^- \gamma$ simulation and $\mu^- \gamma$ data, of which the latter two are shown in Figure 7.6.

In Eq. (7.2), the leading term from theory [Per74] is used as a model of the strong background $B_s(q)$. The π^0 background $B_\pi(q)$ is modeled after simulation, as described in Section 7.3 and depicted in Figure 7.7.

Applying the Eq. (7.4) to $\pi^- \gamma$ data, it turns out that the data are not sufficient to determine all eight model parameters independently which leads to emergence of instabilities, an example of which is presented in Figure 7.9 where two neighbouring kinematic bins with two similar shapes are interpreted quite differently by the fit.

To stabilize the fit, the number of parameters is reduced to seven by means of a dynamic constraint for b_1/b_2 which has been calibrated from $\pi\gamma$ simulation as shown in Figure 7.8:

(a) $\pi^-\gamma$ simulation

(b) $\mu^-\gamma$ data
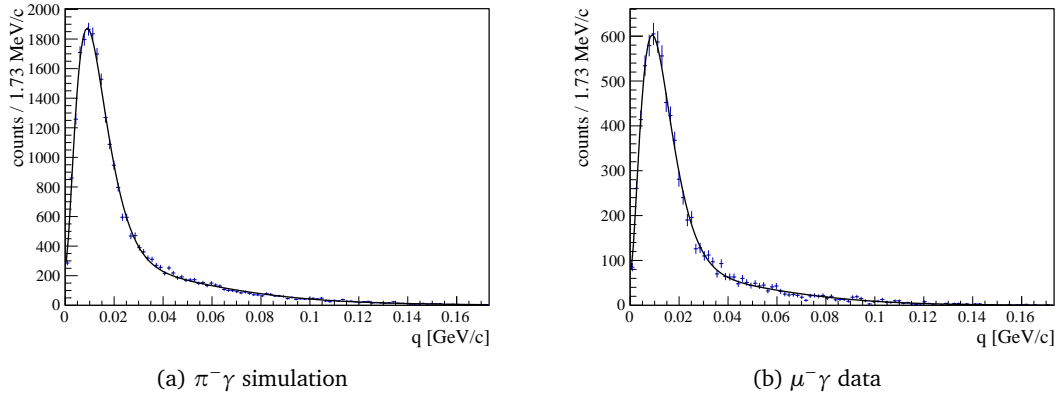
Figure 7.6: tests of Primakoff signal shape $S(q)$
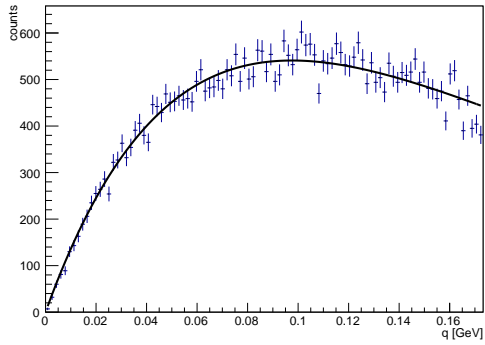

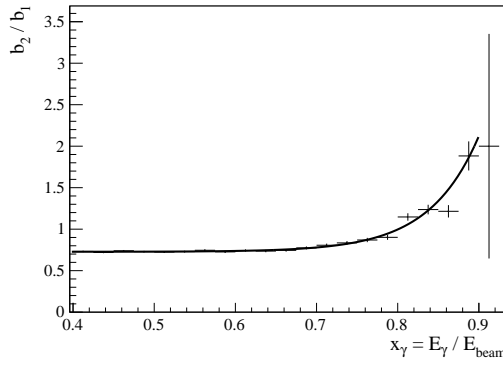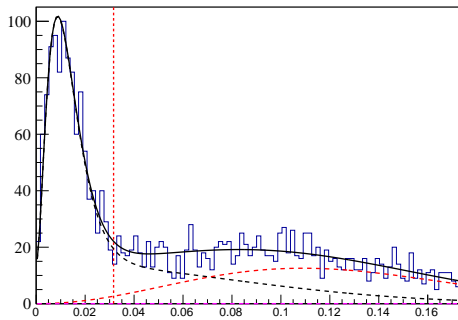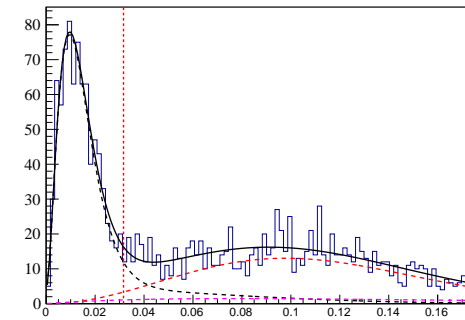Figure 7.7: $\pi^-\pi^0$ simulation fitted with $B_\pi(q)$

Figure 7.8: determination of the b_2/b_1 constraint from $\pi\gamma$ simulation

(a) $0.75 < x_\gamma < 0.775$

(b) $0.775 < x_\gamma < 0.8$

Figure 7.9: instability in 8 parameter fit of M to two neighbouring x_γ bins of $\pi\gamma$ data [dashed black: S, dashed red: B_s, dashed magenta: B_π]

$$b_2 = (0.727540 + 5.11658 \times 10^{-7} \cdot e^{16.4645\,x_\gamma})\,b_1 \qquad (7.5)$$

After placing this constraint, the instabilities are much reduced. Still, the information contained in the q spectra does not seem to be sufficient to separate strong background from π^0 background: The fit shows an undue preference for populating only B_s instead of splitting events among B_s and B_π according to their relative strengths, a typical example being exhibited in Figure 7.10a. Thus, the π^0 background which has been discussed in Section 7.3 is mis-interpreted as strong background. Since both of the backgrounds have similar shapes and both are to be subtracted to obtain the polarizability result, this mis-interpretation among backgrounds does not constitute much of a problem, though.
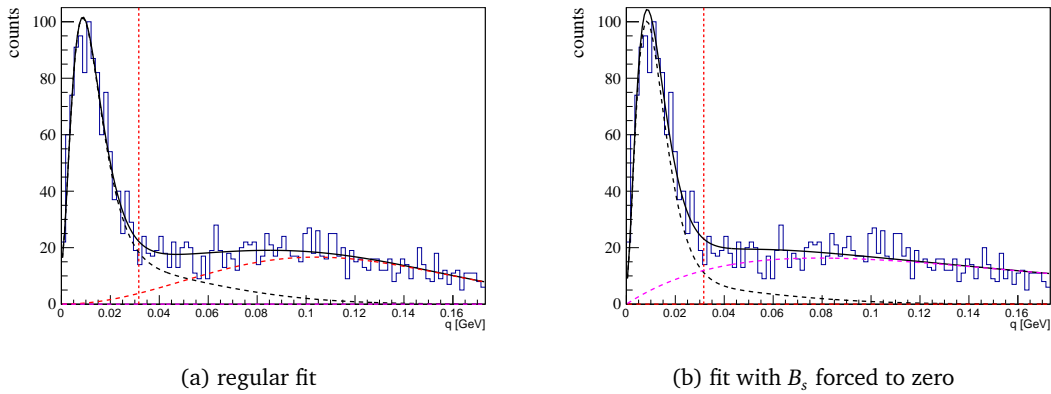

(a) regular fit

(b) fit with B_s forced to zero

Figure 7.10: pion beam data, $0.75 < x_\gamma < 0.775$ [dashed black: S, dashed red: B_s, dashed magenta: B_π]

To estimate the systematic error brought about by the difference of the background shapes, the fits have been re-done with the $B_s(q)$ component forced to zero. As demonstrated in Figure 7.10a, under these circumstances, the full background intensity is attributed to the B_π component.

Using the regular fit, the background correction to the value of the pion polarizability amounts to $-0.4 \times 10^{-4}\,\mathrm{fm}^3$, whereas a correction of $-0.5 \times 10^{-4}\,\mathrm{fm}^3$ is determined via the alternate fit without B_s. This confirms that mis-interpreting one type of background for another has little effect on the polarizability value.

The systematic error of the background subtraction procedure is estimated to be $0.4 \times 10^{-4}\,\mathrm{fm}^3$. This value takes into account the mix-up of different types of backgrounds, possible errors introduced by constraining the fit parameters[1] as well as possible inaccuracies of the models themselves. The error estimate should also be sufficient to cover interference effects between Primakoff reaction and strong background which are expected to be small because of $\pi/2$ phase difference between the terms. Altering the total amount of background by varying the exclusivity cut in the range 10–15 GeV leads to polarizability variations which are consistent with the quoted systematic error.

---

[1]Several different constraints have been tried, the most reliable of which has been presented above. All results obtained that way have been found to lie within the quoted systematic error.
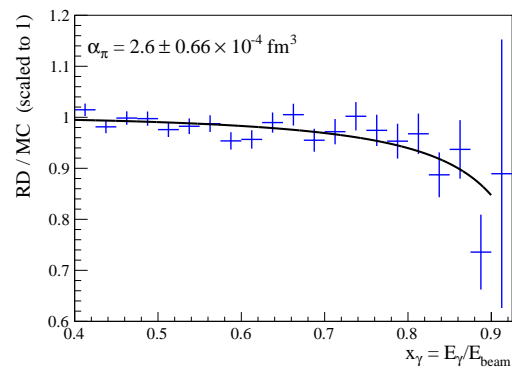
Figure 7.11: Polarizability fit to uncorrected RD/MC ratio.

Chapter 8

Experimental result for the charged pion polarizability
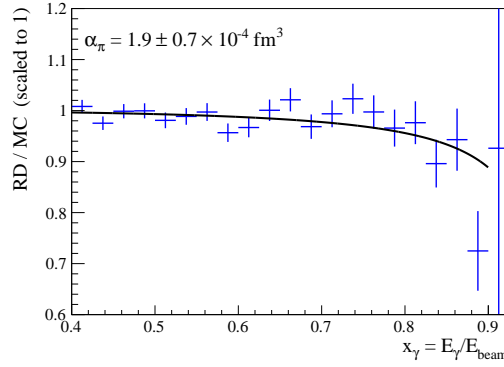
Figure 8.1: Polarizability fit to background-corrected RD/MC ratio.

To obtain the final result, Eq. (5.3) is fitted to the ratio of background-corrected real data divided by simulation as exhibited in Figure 8.1. In that way, the pion polarizability α_π is determined to be:

$$\alpha_\pi = 1.9 \pm 0.7_{\text{stat.}} \times 10^{-4}\,\text{fm}^3 \tag{8.1}$$

The magnitudes of the individual contributions to the systematic error are summarized in Table 8.1. Their detailed description may be found in the sections referenced therein. Since no correlations between the individual errors are known, the total systematic error is computed as the geometric sum of the individual contributions. Thus, the result of the COMPASS 2009 measurement of the pion polarizability, determined under the assumption of $\alpha_\pi + \beta_\pi = 0$ and including random and systematic errors, is given by:

$$\alpha_\pi = 1.9 \pm 0.7_{\text{stat.}} \pm 0.8_{\text{syst.}} \times 10^{-4}\,\text{fm}^3 \tag{8.2}$$

The analysis presented in this work has passed internal peer-review and its outcome has been released as preliminary result by the COMPASS collaboration.

| description	estimated magnitude CL = 68 % [$10^{-4}\,\text{fm}^3$]
tracking (Section 3.7)	0.6
radiative corrections (Section 5.2)	0.3
background subtraction in q (Section 7.5)	0.4
pion electron scattering (Section 7.1)	0.2
quadratic sum	0.8

Table 8.1: sources of systematic errors and magnitudes attributed to them, estimated on 68 % confidence level

8.1 Placement within the empirical and theoretical context

Due to its low magnitude and unprecedented accuracy, the measurement described in this work profoundly impacts the perception of the relation between theory and experiment for the charged pion polarizability. Previously, the individual experiments were well in agreement but together did exhibit serious tension towards the ChPT prediction, accumulating a combined distance of 2.6 standard deviations as discussed in Section 1.1.
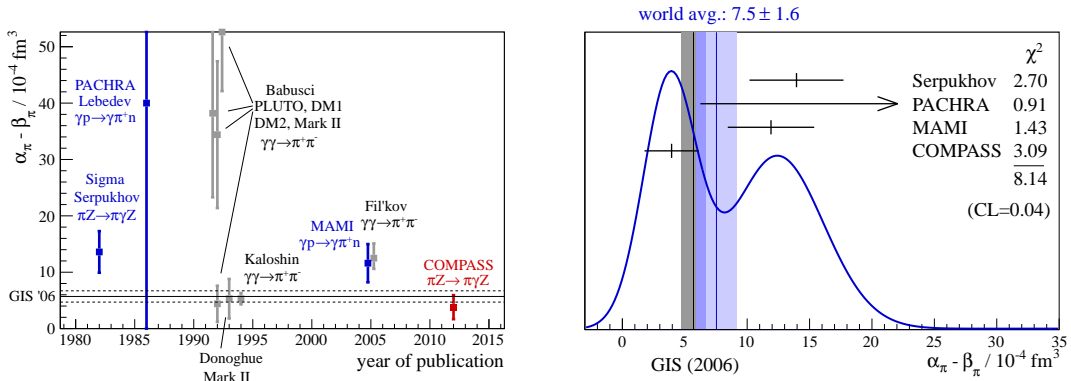
(a) Overview of previous polarizability measurements: Dedicated experimental measurements are shown in colour whereas re-analyses and combined analyses are indicated in grey.

(b) Ideogram of the dedicated experimental measurements in the style used by the Particle Data Group. The quoted confidence level refers to the agreement of the experiments with each other.

Figure 8.2: Previous measurements of $\alpha_\pi - \beta_\pi$: The ChPT prediction by [GIS06] and its error margins are indicated by the solid/dashed lines and the grey band respectively. A more detailed description of the plots is given in Section 1.1 together with the corresponding plots before the COMPASS measurement.

By including the COMPASS result in the world average, this situation is turned upside down: The inconsistency between ChPT and experiments is fully resolved, the remaining distance being a little less than one standard deviation. In return however, relevant discrepancy has arisen between the different measurement which now can be reconciled

only on a χ^2 confidence level of 4.3 % as showcased in Figure 8.2. Consequentially, further measurements would be beneficial to clear up the experimental picture.[1]

Fortunately, a data sample at least four times as large as the one that was analyzed in this work has been recorded over the last months at COMPASS [Gru12] which is expected to yield further insights into the pion polarizabilities by ways of a more precise evaluation of $\alpha_\pi - \beta_\pi$, separate determination of α_π and β_π without the constraint of $\alpha_\pi + \beta_\pi = 0$ and the measurement of quadrupole polarizability terms, polarizability s-dependence and also $\alpha_\pi + \beta_\pi = 0$ kaon polarizability.

---

[1]Possibly, some of the tension can be alleviated if the MAMI data point is to be shifted by the outcome of the ongoing re-analysis in a chiral-invariant framework that is mentioned in [GIS06].

Appendix A

Miscellanea

A.1 RICH pipe tracking issues
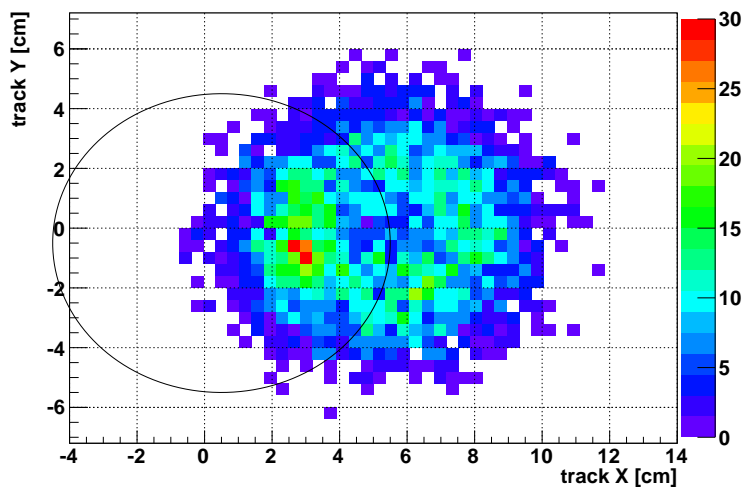
Figure A.1: charged tracks extrapolated to Z position of RICH pipe, position of the pipe indicated in black

In previous data reconstructions, considerable tracking inefficiencies were observed for charged tracks passing the RICH pipe at grazing angles, cf. Figure A.1. This problem was greatly alleviated in the latest "t68/t70" productions by the introduction of special RICH pipe code and by tuning of tracking parameters by [Bed].

A.2 RICH pipe position determination
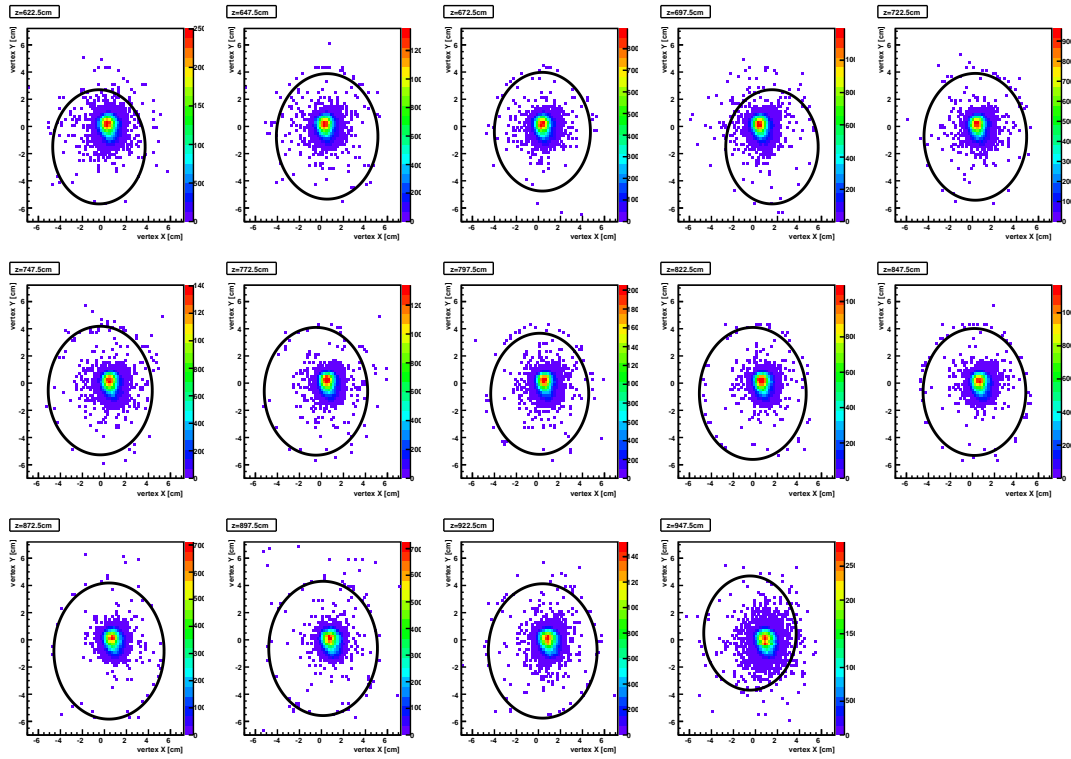
Figure A.2: determination of the position of the RICH pipe by fitting circles to vertex positions in slices of Z

The precise position of the RICH pipe has been determined in this work by fitting circles to vertex positions in slices of Z. (The first, fourth and last fits have failed and thus were not used for the position determination.)

A.3   Polynomial approximation for hadron beam energy determination

In Section 3.5 a method for the determination of the hadron beam energy from beam parameter correlations developed by [Fri12a] and [Krä12] is introduced for which an approximation in polynomial form by [Fri12a] that is useful to avoid time-consuming neural network evaluations is given here:

$$
\begin{aligned}
E = {} & 190.00445 - 1.22949\,Y + 0.894051\,X \\
& + 0.758762\,Y^2 + 0.617662\,X^2 + 0.0766366\,XY \\
& - 0.0637708\,XY^2 + 0.102544\,X^2Y - 0.28268\,X^2Y^2 \\
& + 0.607125\,Y^3 + 0.215115\,X^3 \\
& - 3181.61\,(dY/dZ + 0.746544\,dX/dZ)
\end{aligned}
\tag{A.1}
$$

X and Y are given in cm. The validity range for that polynomial is

$$
\begin{aligned}
|X| &< 1.8 \\
|Y| &< 1.8 \\
|dX/dZ| &< 0.0005 \\
|dY/dZ + 0.0003| &< 0.0005
\end{aligned}
\tag{A.2}
$$

which fully overlaps with the kinematic region that is selected in the polarizability analysis.

A.4 Variation of cuts
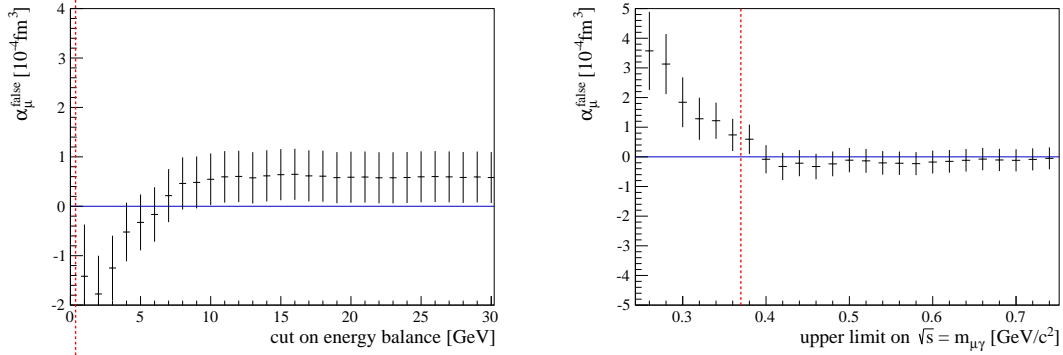
(a) false muon polarizability depending on beam divergence cut

(b) false muon polarizability obtained in slices of beam divergence

Figure A.3: Studies of false muon polarizability: For comparison the cut on hadron beam divergence is indicated by the red dashed line.

A.5 Spectrometer acceptance
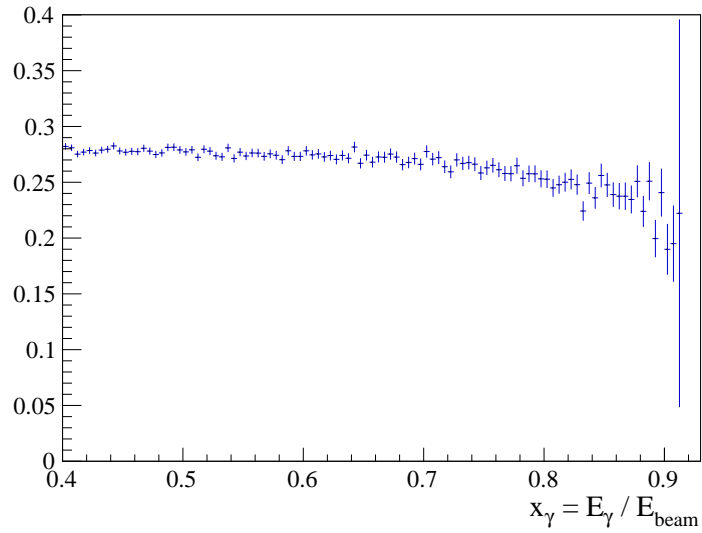
Figure A.4: Spectrometer acceptance for $\pi^-\gamma$ events versus x_γ.

Own Contributions

All of the analysis presented in this work has been conducted by myself and under the skillful supervision of Jan Friedrich except where contributions of others have been indicated in the text. Useful discussions with Alexey Guskov who has performed a cross-check of my analysis are gladly acknowledged.

I was in charge of managing the calorimeter working group at COMPASS which has seen intense activity in 2010 and from within which most of the production-level ECAL2 calibrations described in Section 3.1 have been conceived and implemented. The calibrations documented in Section 3.2 and applied on the analysis level are my own work.

The generator for the simulation of Primakoff-Compton scattering events was created in collaboration: Norbert Kaiser has provided the calculations, Jan Friedrich has implemented their numerical evaluation and I have contributed the sample-and-reject logic and the interfaces to the user and to the COMGEANT simulation package.

On several occasions, I have represented the COMPASS collaboration at international conferences. Also, I have provided plots from my ongoing analysis to be shown to the referees of the SPS Committee in their assessment of the COMPASS experiment.

I have pressed ahead with the internal peer-review of the analysis by giving numerous presentations at various internal meetings, by writing release notes and by holding contact with the COMPASS Publication Committee, all of which has been concluded successfully with the public release of the outcome of my analysis as preliminary result by the COMPASS collaboration this month.

Outside of the scope of this work, I have undertaken an analysis of the anomalous π^0 production in the $\pi^- Z \to \pi^- \pi^0 Z$ process, for which I have attained a kinematic release in March 2008.

Further, I have supervised the master thesis of Talayeh Aledavood (colour transparency, [Ale09]), the diploma thesis of Robert Konopka (online filter, [Kon09]) and the diploma thesis of Julian Taylor (π^0 life time, [Tay11]).

For $4\,1/2$ years I have been in charge of the administration of the E18 computing environment encompassing well over 100 desktop PCs, servers and compute nodes in the E18 batch system.

Continuing the work of my own diploma thesis [Nag05], over the years I've maintained the COMPASS online filter with varying intensity and sorted out troubles blocking data acquisition at COMPASS more than once. Also, I have participated in the design and construction of the first PixelGEM prototype at COMPASS (cf. [Haa12] for a description).

Acknowledgements

Bibliography

[A⁺86]   H. Aihara et al. Pion and Kaon Pair Production in Photon-Photon Collisions. *Phys. Rev. Lett.* **57**, 404 (1986).   *cited on page 2.*

[A⁺07]   P. Abbon et al. The COMPASS experiment at CERN. *Nucl. Instrum. Meth.* **A577**, 455–518 (2007).   *cited on page 7.*

[A⁺12]   C. Adolph et al. First Measurement of Chiral Dynamics in $\pi^- \gamma \to \pi^- \pi^- \pi^+$. *Phys. Rev. Lett.* **108**, 192001 (2012).   *cited on page 46.*

[AAA⁺05]   J. Ahrens, V.M. Alexeev, J.R.M. Annand, H.J. Arends, R. Beck, et al. Measurement of the π^+-meson polarizabilities via the $\gamma p \to \gamma \pi^+ n$ reaction. *Eur. Phys. J.* **A23**, 113–127 (2005).   *cited on page 2.*

[ABB⁺83]   Yu.M. Antipov, V.A. Batarin, V.A. Bessubov, N.P. Budanov, Yu.P. Gorin, et al. Measurement of pi- Meson Polarizability in Pion Compton Effect. *Phys. Lett.* **B121**, 445–448 (1983).   *cited on page 2.*

[ABB⁺85]   Yu.M. Antipov, V.A. Batarin, V.A. Bessubov, N.P. Budanov, Yu.P. Gorin, et al. Experimental Estimation of the Sum of Pion Electrical and Magnetic Polarizabilities. *Z. Phys.* **C26**, 495–497 (1985).   *cited on page 1.*

[ABB⁺86]   T.A. Aibergenov, P.S. Baranov, O.D. Beznisko, S.N. Cherepniya, L.V. Filkov, et al. Radiative photoproduction of pions and pion Compton scattering. *Czech. J. Phys.* **B36**, 948–951 (1986).   *cited on page 2.*

[ABD⁺80]   H.W. Atherton, C. Bovet, N. Doble, G. von Holtey, L. Piemontese, et al. Precise Measurements of Particle Production by 400 GeV/c Protons on Beryllium Targets, 1980.   *cited on pages 9 and 46.*

[Ale09]   Talayeh Aledavood. Studies of Color Transparency Using Di-jet Events from a 190 GeV/c Pion Beam Scattered on Various Targets at COMPASS, 2009. Master's thesis.   *cited on page 63.*

[B⁺84]   Christoph Berger et al. Pion pair production in photon-photon interactions. *Z. Phys.* **C26**, 199 (1984).   *cited on page 2.*

[B⁺92]   H.J. Behrend et al. An experimental study of the process $\gamma\gamma \to \pi^+\pi^-$. *Z. Phys.* **C56**, 381–390 (1992).   *cited on page 2.*

[B⁺96]   Günter Baum et al. COMPASS: A Proposal for a Common Muon and Proton Apparatus for Structure and Spectroscopy. (1996).   *cited on page 4.*

[B⁺12a]   J. Beringer et al. Review of Particle Physics (RPP). *Phys. Rev.* **D86**, 010001 (2012).   *cited on page 46.*

[B⁺12b]   Johannes Bernhard et al. 2009: Test DST Productions, `http://wwwcompas s.cern.ch/twiki/bin/view/Trigger/HadronTrigger`. (unpublished).   *cited on page 13.*

[BBG⁺90] J. Boyer, F. Butler, G. Gidal, G. Abrams, D. Amidei, et al. Two photon production of pion pairs. *Phys. Rev.* **D42**, 1350–1367 (1990).   *cited on page 2.*

[BBG⁺92] D. Babusci, S. Bellucci, G. Giordano, G. Matone, A.M. Sandorfi, et al. Chiral symmetry and pion polarizabilities. *Phys. Lett.* **B277**, 158–162 (1992). *cited on pages 2 and 3.*

[Bed]   Yann Bedfer. Private communication.   *cited on pages 32 and 59.*

[Ber07]   A.M. Bernstein. Opening Remarks at Chiral Dynamics 2006: Experimental Tests of Chiral Symmetry Breaking. (2007).   *cited on page 2.*

[Bic11]   Karl Bicker. Construction and Commissioning of a Cooling and Support Structure for the Silicon Detectors for the COMPASS Experiment, 2011. diploma thesis.   *cited on page 11.*

[Bis]   Jens Bisplinghoff. Private communication.   *cited on page 10.*

[BMP78]   C. Bovet, S. Milner, and A. Placci. The Cedar Project. Cherenkov Differential Counters with Achromatic Ring Focus. *IEEE Trans. Nucl. Sci.* **25**, 572–576 (1978).   *cited on page 10.*

[BMP⁺82] C. Bovet, R. Maleyran, L. Piemontese, A. Placci, and M. Placidi. The CEDAR counters for particle identification in the SPS secondary beams: a description and an operation manual. (1982).   *cited on page 10.*

[Bür96]   Urs Bürgi. Pion polarizabilities and charged pion pair production to two loops. *Nucl. Phys.* **B479**, 392–426 (1996).   *cited on page 1.*

[CER]   Cern, `http://cern.ch`.   *cited on page 7.*

[COM12]   COMPASS. *The COMPASS setup for physics with hadron beams*. (in preparation), 2012.   *cited on pages 7, 8, and 12.*

[COR]   Coral web site, `http://coral.cern.ch/`.   *cited on page 14.*

[DH93]   John F. Donoghue and Barry R. Holstein. Photon-photon scattering, pion polarizability, and chiral symmetry. *Phys. Rev.* **D48**, 137–146 (1993). *cited on pages 2 and 3.*

[Din10]   Anna-Maria Dinkelbach. Precision Tracking and Electromagnetic Calorimetry Towards a Measurement of the Pion Polarizabilities at COMPASS, 2010. PhD thesis.   *cited on page 5.*

[E18]   E18 computing web site,
            http://www.e18.ph.tum.de/research/computing/.   *cited on page 14.*

[Fis12]   Horst Fischer. Private communication, 2012.   *cited on page 30.*

[FK06]   L.V. Fil'kov and V.L. Kashevarov. Determination of $\pi^\pm$ meson polarizabilities
            from the $\gamma\gamma \to \pi^+\pi^-$ process. *Phys. Rev.* **C73**, 035210 (2006).   *cited on page 2.*

[FK12]   Jan Michael Friedrich and Markus Krämer. Reconstruction of the Pion Beam
            Energy from Beam Optics. *COMPASS Note 2012-02* (2012). (unpublished).
                                                                                          cited on page 22.

[Fri10]   Jan Michael Friedrich. CEDAR performance 2009. *COMPASS Note 2010-15*
            (2010). (unpublished).   *cited on pages 30 and 45.*

[Fri12a]   Jan Michael Friedrich. Private communication, 2012.   *cited on pages 10, 22, 38,*
            and 61.

[Fri12b]   Jan Michael Friedrich. Chiral Dynamics in Pion-Photon Reactions, 2012.
            Habilitation treatise.   *cited on pages 3 and 38.*

[G$^+$10]   Fabrice Gautheron et al. COMPASS-II Proposal. (2010).   *cited on page 5.*

[Gas09]   Jürg Gasser. On the history of pion-pion scattering. *Proceedings of Science*
            EFT09, 029 (2009).   *cited on page 1.*

[Gat]   Lau Gatignon. Private communication.   *cited on page 10.*

[Gen11]   Armin Gensler. Private communication, 2011.   *cited on page 30.*

[Ger12]   Sergei Gerassimov. Private communication, 2012.   *cited on pages 15 and 16.*

[GIS06]   Jürg Gasser, Mikhail A. Ivanov, and Mikko E. Sainio. Revisiting $\gamma\gamma \to \pi^+\pi^-$
            at low energies. *Nucl. Phys.* **B745**, 84–108 (2006).   *cited on pages 1, 2, 3, 56, and 57.*

[GM80]   A.S. Galperin and Guenakh Mitselmakher. Calculation of Ultrarelativistic
            Pion Bremsstrahlung Cross Section on Nuclei with the Allowance for Pion
            Polarization. *Yadernaya Fiz.* (1980).   *cited on page 37.*

[Gra12]   Stefanie Grabmüller. Cryogenic Silicon Detectors and Analysis of Primakoff
            Contributions to the Reaction $\pi^-\text{Pb} \to \pi^-\pi^-\pi^+\text{Pb}$ at COMPASS, 2012. PhD
            thesis.   *cited on page 11.*

[Gru12]   Boris Grube. Private communication, 2012.   *cited on page 57.*

[Gus10]   Alexey Guskov. Analysis of the charged pion polarizability measurement
            method at COMPASS experiment, 2010. PhD thesis.   *cited on page 5.*

[Gus11]   Alexey Guskov. Private communication, 2011.   *cited on pages 9 and 47.*

[H$^+$03]   A. Heister et al. Exclusive production of pion and kaon meson pairs in two
            photon collisions at LEP. *Phys. Lett.* **B569**, 140–150 (2003).   *cited on page 2.*

[Haa12]   Florian Haas. Precision Meson Spectroscopy: Diffractive Production at
             COMPASS and Development of a GEM Detector with pixelised Readout,
             2012. PhD thesis (in preparation).   *cited on page 63.*

[HFK⁺11]   Stefan Huber, Jan Friedrich, Bernhard Ketzer, Igor Konorov, Markus Kramer,
             et al. A Digital Trigger for the Electromagnetic Calorimeter at the COMPASS
             Experiment. *IEEE Trans. Nucl. Sci.* **58**, 1719–1722 (2011).   *cited on pages 13 and 14.*

[Hof56]   Robert Hofstadter. Electron Scattering and Nuclear Structure.
             Rev. Mod. Phys. **28**, 214–254 (1956).   *cited on page 39.*

[Hub12]   Stefan Huber. Private communication, 2012.   *cited on page 30.*

[Jas12]   Prometeusz Jasinski. Analysis of diffractive dissociation of K^- into $K^- \pi^+ \pi^-$
             on a liquid hydrogen target at the COMPASS spectrometer, 2012. PhD thesis.
                                                                      cited on pages 11 and 30.

[Kon09]   Robert Konopka. Real time data processing and feature extraction of
             calorimeter data in compass, 2009. diploma thesis.   *cited on page 63.*

[Krä12]   Markus Krämer. Private communication, 2012.   *cited on pages 10, 22, and 61.*

[KS94]   A.E. Kaloshin and V.V. Serebryakov. π^+ and π^0 polarizabilities from $\gamma\gamma \to \pi\pi$
             data. *Z. Phys.* **C64**, 689–694 (1994).   *cited on page 2.*

[Ku01]   Roland Kuhn. Simulations for the measurement of the polarizabilities of the
             pion at COMPASS, 2001. diploma thesis.   *cited on page 4.*

[Lee11]   Michael Leeb. Optimization of the Clustering and Tracking Algorithms of the
             Silicon Microstrip Detectors for the COMPASS Experiment, 2011. diploma
             thesis.   *cited on page 11.*

[Leu94]   Heinrich Leutwyler. On the Foundations of Chiral Perturbation Theory.
             Annals Phys. **235**, 165–203 (1994).   *cited on page 1.*

[M2]   The M2 beam line for COMPASS, `http://sba.web.cern.ch/sba/Beams`
             `AndAreas/M2/M2-OperatorCourse.pdf`.
             cited on page 9.

[MAB⁺90]   H. Marsiske, D. Antreasyan, H.W. Bartels, et al. Measurement of $\pi^0 \pi^0$
             production in two-photon collisions. *Phys. Rev.* **D41**, 3324–3334 (1990).
             cited on page 2.

[MP87]   D. Morgan and M.R. Pennington. Low $\gamma\gamma \to \pi\pi$ cross-section and the QED
             Born amplitude. *Phys. Lett.* **B192**, 207–211 (1987).   *cited on pages 2 and 3.*

[N⁺05]   H. Nakazawa et al. Measurement of the $\gamma\gamma \to \pi^+ \pi^-$ and $\gamma\gamma \to K^+ K^-$
             processes at energies of 2.4 GeV to 4.1 GeV. *Phys. Lett.* **B615**, 39–49 (2005).
             cited on page 2.

[N⁺10]   K. Nakamura et al. Review of Particle Physics. *J. Phys. G* **G37**, 075021
             (2010).   *cited on page 3.*

[Nag05]   Thiemo Nagel. Cinderella: an Online Filter for the COMPASS experiment, 2005. diploma thesis.   *cited on page 63.*

[NBG12]   Thiemo Nagel, Yann Bedfer, Rumen Gushterski, and Alexander Austregesilo. 2009: Test DST Productions, `http://wwwcompass.cern.ch/twiki/bin/view/HadronAnalysis/TestProduction2009`. (unpublished).
            cited on page 14.

[NFP08]   Thiemo Nagel, Jan Michael Friedrich, and Stephan Paul. 2004 hadron data: Investigating beam k^- decays for fun and profit, 2008. Presented at Nov. 2008 COMPASS offline meeting (unpublished).   *cited on pages 9 and 46.*

[NG12]   Thiemo Nagel and Alexey Guskov. 2009 bad spill list, `http://wwwcompass.cern.ch/twiki/bin/view/HadronAnalysis/BadSpills2009`. (unpublished).   *cited on page 27.*

[NuD12]   National Nuclear Data Center. Nudat 2 database, `http://www.nndc.bnl.gov/nudat2/`.   *cited on page 11.*

[Pen95]   M.R. Pennington. What we learn by measuring $\gamma\gamma \to \pi\pi$ at DAΦNE. (1995).   *cited on pages 2 and 3.*

[Per74]   M. L. Perl. *High energy hadron physics*. Wiley-Interscience publications. Wiley, 1974.   *cited on page 50.*

[PHA]   Phast web site, `http://ges.home.cern.ch/ges/phast/`.   *cited on page 14.*

[Pol]   Vladimir Polyakov. Private communication.   *cited on page 12.*

[Pri51]   Henry Primakoff. Photo-Production of Neutral Mesons in Nuclear Electric Fields and the Mean Life of the Neutral Meson. *Phys. Rev.* **81**, 899 (1951).
            cited on page 3.

[ROO]   Root web site, `http://root.cern.ch/`.   *cited on page 14.*

[S⁺11]   Tobias Schlüter et al. Large-Area Sandwich Veto Detector with WLS Fibre Readout for Hadron Spectroscopy at COMPASS. *COMPASS Note 2011-03* (2011). (unpublished).   *cited on page 13.*

[SDD⁺11]   T. Schlüter, W. Dünnweber, K. Dhibar, M. Faessler, R. Geyer, et al. Large-Area Sandwich Veto Detector with WLS Fibre Readout for Hadron Spectroscopy at COMPASS. *Nucl. Instrum. Meth.* **A654**, 219–224 (2011).   *cited on page 13.*

[Tay11]   Julian Taylor. Measuring the π^0 lifetime at the compass experiment—a feasibility study, 2011. diploma thesis.   *cited on page 63.*

[Uhl]   Sebastian Uhl. Private communication.   *cited on page 16.*

[vH02]   Martin Frhr. v. Hodenberg. *A First Reconstruction of COMPASS Data*. diploma thesis, Albert-Ludwigs-Universität Freiburg, 2002.   *cited on page 9.*

[VJV87]   H. De Vries, C.W. De Jager, and C. De Vries. Nuclear charge and magnetization density distribution parameters from elastic electron scattering. *Atom. Data Nucl. Data Tabl.* **36**, 495–536 (1987).   *cited on page 39.*

[vW34]   C.F. von Weizsäcker. Radiation emitted in collisions of very fast electrons. *Z. Phys.* **88**, 612–625 (1934).   *cited on page 3.*

[Wei68]   Steven Weinberg. Nonlinear realizations of chiral symmetry. *Phys. Rev.* **166**, 1568–1577 (1968).   *cited on page 1.*

[Wil34]   E.J. Williams. Nature of the high-energy particles of penetrating radiation and status of ionization and radiation formulae. *Phys. Rev.* **45**, 729–730 (1934).   *cited on page 3.*

[Y$^+$95]   Fumiaki Yabuki et al. Study of $\pi^+\pi^-$ pair production in a two photon process at TRISTAN. *J. Phys. Soc. Jap.* **64**, 435–447 (1995).   *cited on page 2.*

[Zim11]   Philipp Zimmerer. Performance of cryogenic silicon microstrip detectors at the COMPASS experiment, 2011. diploma thesis.   *cited on page 11.*